

# Fiber Scaffold Patterning for Mending Hearts: 3D Organization Bringing the Next Step

Marleen Kristen,\* Madison J. Ainsworth,\* Nino Chirico, Casper F. T. van der Ven, Pieter A. Doevendans, Joost P. G. Sluijter, Jos Malda, Alain van Mil,\* and Miguel Castilho\*

Heart failure (HF) is a leading cause of death worldwide. The most common conditions that lead to HF are coronary artery disease, myocardial infarction, valve disorders, high blood pressure, and cardiomyopathy. Due to the limited regenerative capacity of the heart, the only curative therapy currently available is heart transplantation. Therefore, there is a great need for the development of novel regenerative strategies to repair the injured myocardium, replace damaged valves, and treat occluded coronary arteries. Recent advances in manufacturing technologies have resulted in the precise fabrication of 3D fiber scaffolds with high architectural control that can support and guide new tissue growth, opening exciting new avenues for repair of the human heart. This review discusses the recent advancements in the novel research field of fiber patterning manufacturing technologies for cardiac tissue engineering (cTE) and to what extent these technologies could meet the requirements of the highly organized and structured cardiac tissues. Additionally, future directions of these novel fiber patterning technologies, designs, and applicability to advance cTE are presented.


failure imposes an enormous burden on society.<sup>[1]</sup> Despite major advances in cardiovascular therapy, there is still no cure available for the rapidly increasing HF-patient population. A few of the most common causes of HF progression are ischemic heart disease, hypertension and valve disorders.<sup>[2]</sup> The result of these events is an altered structure and function of the heart, impairing the heart's contractility and/or pump function. In the case of myocardial infarction, up to a billion of cardiomyocytes (CM) are lost.<sup>[3]</sup> This loss of CMs is considered to be irreversible in the adult human heart, as the regenerative capacity of the myocardium is extremely limited.<sup>[4]</sup> The damaged myocardium is replaced by a noncontractile, fibrotic scar resulting in a loss of pump function through a remodeling process involving myocardial cell death, an inflammatory response, fibrosis, myocyte hypertrophy, and

## 1. The Failing Heart

Heart failure (HF) is a leading cause of morbidity and mortality for both men and women worldwide. With an estimated worldwide prevalence of 26 million patients and a severe prognosis of 50% mortality within five years, heart

chamber dilation, leading to cardiac dysfunction and ultimately heart failure. To date, the only viable curative therapy for patients with end-stage HF is heart transplantation. However, due to organ donor shortage, heart transplantation is unavailable for most patients and not realistic as a standard therapy.<sup>[5]</sup>

M. Kristen, M. J. Ainsworth, N. Chirico, C. F. T. van der Ven, Prof. J. P. G. Sluijter, Prof. J. Malda, Dr. A. van Mil, Dr. M. Castilho  
Regenerative Medicine Center  
University Medical Center Utrecht  
Utrecht 3584 CT, The Netherlands  
E-mail: m.kristen@students.uu.nl; M.J.Ainsworth-2@umcutrecht.nl;  
A.vanMil@umcutrecht.nl; M.DiasCastilho@umcutrecht.nl  
M. Kristen, M. J. Ainsworth, Prof. J. Malda, Dr. M. Castilho  
Department of Orthopedics  
University Medical Center Utrecht  
Utrecht 3584 CX, The Netherlands

 The ORCID identification number(s) for the author(s) of this article can be found under <https://doi.org/10.1002/adhm.201900775>.

© 2019 The Authors. Published by WILEY-VCH Verlag GmbH & Co. KGaA, Weinheim. This is an open access article under the terms of the Creative Commons Attribution-NonCommercial License, which permits use, distribution and reproduction in any medium, provided the original work is properly cited and is not used for commercial purposes.

N. Chirico, C. F. T. van der Ven, Prof. P. A. Doevendans, Prof. J. P. G. Sluijter, Dr. A. van Mil  
Department of Cardiology  
Experimental Cardiology Laboratory  
University Medical Center Utrecht  
Utrecht 3584 CX, The Netherlands  
Prof. P. A. Doevendans, Dr. A. van Mil  
Netherlands Heart Institute  
Utrecht 3511 EP, The Netherlands  
Prof. J. Malda  
Department of Equine Sciences  
Faculty of Veterinary Medicine  
Utrecht University  
Utrecht 3584 CL, The Netherlands  
Dr. M. Castilho  
Department of Biomedical Engineering  
Eindhoven University of Technology  
Eindhoven 5612 AE, The Netherlands

DOI: 10.1002/adhm.201900775

Heart failure itself can also be caused by valve disorders, with calcific aortic valve disease (CAVD) being the most common valvular heart disease.<sup>[6]</sup> Early stage CAVD without obstruction of blood flow (aortic valve sclerosis) can progress to obstructive aortic valve stenosis, resulting in an increase of mechanical stress on the left ventricle, thereby reducing cardiac output and function.<sup>[7]</sup> Ventricular assist devices (VADs) are widely available and have successfully been used as a bridge to heart transplantation, providing functional support to the damaged heart. However, these devices do not offer a permanent solution as they are burdened with increased thrombotic events, bleeding, and infection, as well as lacking the capacity to adapt to patient variability.<sup>[8]</sup> For cardiac valves specifically, mechanical and bioprosthetic valve replacements are the current standard of care for advanced CAVD.<sup>[9]</sup> However, mechanical valves suffer from risk of thrombosis and bleeding, and patients require lifelong anti-coagulation therapy.<sup>[10]</sup> Bioprosthetic valves, typically obtained from bovine or porcine donors, do not suffer from thrombosis risks, but these can suffer from infection, inflammation, or calcification.<sup>[11,12]</sup> For coronary artery disease, obstructed coronary arteries are currently alleviated by percutaneous coronary intervention and stent placement, or coronary artery bypass grafting (CABG) in the case of extensive blockage.<sup>[13]</sup> For CABG, autologous vessels, such as the internal thoracic artery and the great saphenous vein, comprise the gold standard grafts for small-diameter vessels, and currently outperform synthetic alternatives.<sup>[14]</sup> However, they require invasive surgery for harvesting, emphasizing the clinical need for artificial, small-diameter (<6 mm) vessels with compatible mechanical and functional properties to match that of healthy coronary vessels.<sup>[15]</sup>

It is therefore evident that there is a great need for the development of novel techniques to repair injured myocardium, replace damaged valves and treat coronary artery disease. As a result of this need, the beginning of the 21st century has been marked by the rise of reparative treatment strategies for the diseased heart. While first attempts were focused on cell transplantation therapies and major advances in optimizing these strategies have been made, the clinical outcome of cell-based therapy remains extremely unsatisfactory.<sup>[16–18]</sup> An example of alternative approaches to enhance stem cell delivery is the use of microcarriers,<sup>[19–21]</sup> however this does not account for the loss or disarray of the extracellular matrix (ECM) and most importantly, the mechanical properties that are affected in such pathologies. Engineered cardiac tissues designed to mimic the morphological and functional characteristics of native cardiac tissues could provide the answer to enhance cell engraftment compared with direct cell injection.<sup>[22,23]</sup> One cTE strategy that has progressed since its discovery is the scaffold-free cell sheet technology in which cells produce their own ECM.<sup>[24,25]</sup> While this is potentially a beneficial technique for the delivery of cells to the heart tissue, their clinical applicability for cardiac tissue repair, or replacement, is limited due to the frailty of these cell sheets making them prone to damage during the hemodynamic forces in these tissues. Alternatively, cells have also been embedded in synthetic or natural-derived hydrogels, such as poly(ethylene glycol), collagen or fibrin, which can enable physical retention of cells at the target site and reduce cell death.<sup>[23,26]</sup> Nevertheless, the most common hydrogels do not have adequate mechanical



**Madison Ainsworth** is a Ph.D. candidate at the Regenerative Medicine Center, Utrecht (the Netherlands). She obtained her M.Sc. in biofabrication at the Universiteit Utrecht in early 2019 on the development of bioengineered myocardial constructs. Previously, she attained a B.BiomedSc. majoring in anatomical

sciences from the Queensland University of Technology (Australia). Madison's research interests are focused on biofabrication and additive manufacturing techniques for advanced mimicking of native, healthy tissue.



**Alain van Mil** is an assistant professor in the Regenerative Medicine Center Utrecht. He obtained his Ph.D. in 2012 at the University Medical Center Utrecht on the role of non coding RNAs in cardiac regenerative medicine and subsequently did a postdoctoral training in Sanford-Burnham, La Jolla, CA. Since 2016, he is heading

the Circulatory Health Regenerative Medicine Laboratory in the Regenerative Medicine Center Utrecht, where he established the induced pluripotent stem cell facility. His research interests focus on cardiac tissue engineering and advanced human cardiovascular disease modelling using iPS technology and 3D printing.



**Miguel Castillo** received his Ph.D. cum laude in biomedical engineering (2015) from the University of Lisbon, Portugal. He is currently an assistant professor at the University Medical Center Utrecht and a Guest Researcher at the Eindhoven University of Technology. His research focuses on innovating multi-scale design strategies and

bio fabrication processes for the fabrication of functional biomimetic tissues for regenerative medicine applications.

properties to withstand the high dynamic mechanical environment occurring during each cardiac cycle.

Another approach that has received significant attention is the development of supporting scaffolds that could provide mechanical support to the cells while guiding their growth and organization.<sup>[27,28]</sup> Different manufacturing techniques have been investigated for scaffold manufacturing like gas

foaming,<sup>[29]</sup> lyophilization,<sup>[30]</sup> laser ablation,<sup>[31]</sup> selective laser sintering,<sup>[32]</sup> and electrospinning.<sup>[27,33]</sup> Although each of these methods has its benefits for tissue reconstruction, most of them produce dense scaffolds that do not mimic the well-organized microenvironment of the native ECM fibrillar structure. One promising approach is the use of fiber patterning technologies that enable the controlled deposition of fibers, with dimensions down to the cell size, and their assembly in highly organized scaffolds with micro (and even nano) features. These scaffolds create a 3D support and delivery system for cells and allow for the integration of controllable biochemical, topographical, and mechanical cues.<sup>[34]</sup> As a result, these technologies produce instructive structures that can potentially mimic important features of the native ECM fibrillar structure, e.g., support the maturation of stem cell-derived cardiac cells, capture the highly dynamic mechanical properties and tissue organization of the myocardium, vasculature and valves.<sup>[34,35]</sup>

This review systematically discusses the recent advancements of fiber patterning technologies and their potential in cardiac TE. We first recapitulate the characteristics of native myocardial, valve, and vascular tissues as a background to understand the key design requirements and properties of a fiber scaffold. Special focus is given to cell populations, functions and disease, as well as to the native tissue architecture, and mechanical properties. We next provide a detailed review on existent fiber fabrication technologies, their key processing parameters and materials. Subsequently, we present the application of patterned fiber scaffolds in cTE and provide a critical discussion on how such organized fiber scaffolds could meet the cardiac tissue requirements and enhance neo tissue-like formation with native-like characteristics. Finally, we conclude with the future directions of using patterned fiber scaffolds in cTE and their translational potential toward the clinical arena.

## 2. Design Criteria for cTE: Composition and Biomechanics of Cardiac Tissue

### 2.1. Myocardial Tissue Characteristics

The myocardium is the middle and thickest layer of heart tissue between the endocardial and epicardial layers (**Figure 1A**). It is composed of muscular tissue which is specific to the heart (cardiac muscle) and is coordinated into a rhythmic contraction and relaxation pattern initiated by a self-depolarizing (pacemaker) system made of muscle cell fibers specialized for electric conduction. The contractile myocardium is a highly vascularized tissue with a dense capillary network required for a continuous supply of oxygen and nutrients. On the cellular level, the myocardium tissue consists mainly of CMs, fibroblasts (FBs), and endothelial cells (ECs), which are tightly packed within an ECM structure.<sup>[36]</sup> CMs are the key functional unit of the myocardium whereby electrical excitation is linked to calcium-induced mechanical contraction where myosin activation and consequent actin filament shortening results in larger-scale tissue contraction, controlling the filling and ejection of blood by the heart.<sup>[37]</sup> Next to CMs, both FBs and ECs are essential for heart homeostasis, as FBs produce the ECM and therefore provide the structural network and geometrical orientation of

the tissue, and ECs constitute the intricate capillary network throughout the myocardial tissue, providing constant nutrient supply necessary for CM function. The volume fraction occupied by CMs, ECs, and interstitial cells is assessed at 70–80%, 3.2–5.3%, and 1.4–1.9%, respectively.<sup>[36,38]</sup>

The ability of the myocardium to contract and function as a pump is dependent on the muscle's complex structure in which the CMs are parallelly aligned and the ECM provides structural and mechanical support.<sup>[39]</sup> The myocardial ECM consists of fibrous proteins, predominantly collagen type I and II and elastins, carbohydrates, growth factors, and glycoproteins, including fibronectin and proteoglycans.<sup>[39,40]</sup> The human cadaveric decellularized myocardial ECM matrix is reportedly made up of the following ECM volume fraction; collagens (29%), laminins (25.4%), fibrillins (15.6%), and proteoglycans (14.1%), with the rest corresponding to nonmatrix proteins.<sup>[41]</sup> The key constituent of the ECM, collagen, exists as three different fiber types within the myocardium. First, epimysial fibers surround, and tightly constrain the bundles of the myocardium to provide external support. These epimysial collagen fibers have diameters of several micrometers. Second, perimysial fibers are wavy in shape and surround groups of CMs parallelly. They are  $\approx 1 \mu\text{m}$  thick, thereby providing the perimysium with resistance to traction. Lastly, endomysial fibers wrap around individual CMs directing their alignment and providing mechanical support for the cells. These endomysial collagen fibers are the smallest in diameter (20–100 nm).<sup>[39,42]</sup> The densely packed fibers form a tunnel-like structure with 40  $\mu\text{m}$  honeycomb-like cross-section.<sup>[43,44]</sup> This organization assists CMs to rapidly propagate depolarizing electrical signals via gap junctions resulting in synchronous myocardial contractions.<sup>[45]</sup> In addition to its biochemical properties, the ECM's mechanical properties are equally important, affecting cell behavior through, e.g., shear stresses, which are known to affect cell activation, adhesion, and signaling.<sup>[46]</sup> The combination of the myocardial ECMs organization and its mechanically active cellular content results in highly variable mechanical properties throughout the cardiac cycle. While passive myocardium shows most of the mechanical properties characteristic of soft tissues,<sup>[47]</sup> mechanical testing has shown that the stiffness of the healthy left ventricle is  $< 4 \text{ kPa}$  at end diastole and  $\approx 16 \text{ kPa}$  at end systole,<sup>[48]</sup> whereas in the diseased heart in presence of fibrosis the stiffness can even increase to 30–50 kPa.<sup>[49]</sup> Additionally, the myocardium shows anisotropic mechanical properties consistent with cell and fiber orientations. Diffusion tensor imaging and fiber tracking has shown that the muscle fiber angle varies slightly between different transmural layers of the myocardium,<sup>[50–53]</sup> resulting in ventricular torsion allowing efficient ventricular ejection and filling. Another important biomechanical feature of the myocardium originates in the CMs which are longitudinally shortened but axially expanded upon contraction, making myocardial elastic deformations finite and near isochoric.

### 2.2. Cardiac Valve Characteristics

The four cardiac valves facilitate unidirectional blood flow. They are distinguished as semilunar valves prohibiting retrograde flow during diastole (i.e., the aortic and pulmonary valves), and

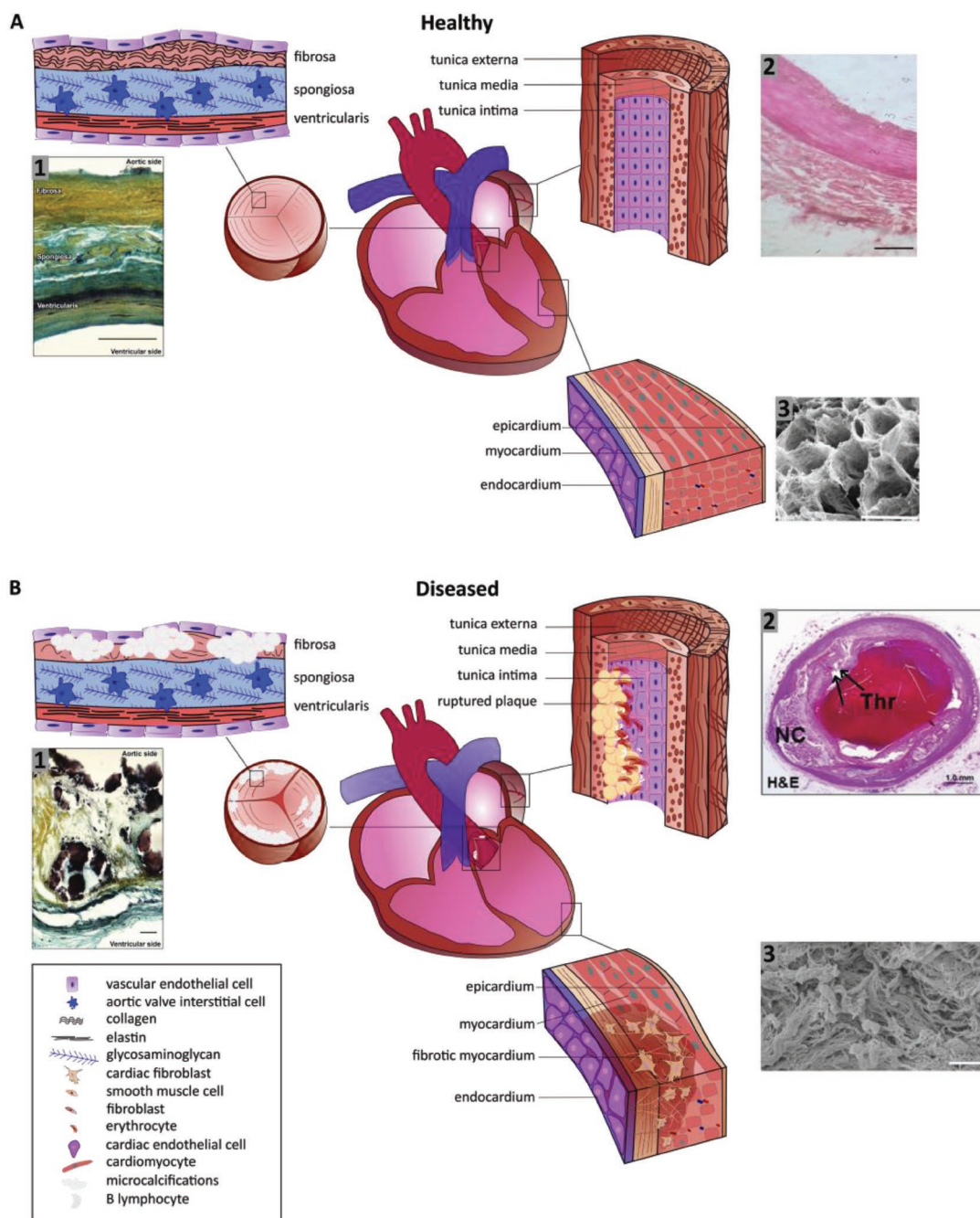


**Figure 1.** Schematic representations of A) the healthy heart with enlargements of the aortic valve highlighting the layer composition, of the coronary arteries outlining the fiber orientation in the tunica, and of the myocardial wall with cellular and fiber direction, and B) the diseased heart illuminating fiber disruptions in the aortic valve due to (micro)calcification, in the coronary arteries due to plaque formation, and in the myocardium due to fibrosis. A1) Movat's pentachrome staining of structural organization in a circumferential cross-section of a human aortic valve leaflet. Yellow = collagen, blue = glycosaminoglycans (GAGs), black = elastin, dark brown/black = calcification. Trilayered structure of the fibrosa (collagen-rich), spongiosa (GAG-rich), and ventricularis (elastin-rich) layers (scale bar = 100 μm). Reproduced with permission under the terms of the CC BY 4.0 license.<sup>[194]</sup> Copyright 2018, the Authors, Published by MDPI. A2) Histology section of coronary arterial wall highlighting the fiber structure and orientation (scale bar = 10 μm). Reproduced with permission under the terms of the CC BY 4.0 license.<sup>[195]</sup> Copyright 2018, the Authors, Published by MedWin Publishers. A3) Scanning electron microscopy photograph displaying the honeycomb-like structure of supportive fibers in the myocardium cross-section (scale bar = 50 μm). Reproduced with permission.<sup>[43]</sup> Copyright 2016, JoVE. B1) Movat's pentachrome staining of structural organization in a circumferential cross-section of a human aortic valve highlighting the disruption of the leaflet layers by calcifications (black) and fibrosis (yellow regions) in CAVD (scale bar = 50 μm). Reproduced with permission under the terms of the CC BY 4.0 license.<sup>[194]</sup> Copyright 2018, the Authors, Published by MDPI. B2) Histology section of coronary arterial wall highlighting the plaque rupture with acute luminal thrombus (Thr) and underlying large necrotic core (NC). Arrows indicate the site of fibrous cap disruption (scale bar = 50 μm). Reproduced with permission.<sup>[196]</sup> Copyright 2013, Elsevier. B3) Scanning electron microscopy photograph showing the randomly arranged bundles of collagen fibres after myocardial infarction and myocardial scarring inside left ventricle (scale bar = 10 μm). Reproduced with permission.<sup>[197]</sup> Copyright 2017, Springer.

atrioventricular valves that prevent back flow during systole (i.e., the mitral/bicuspid and tricuspid valves). The valves primarily consist of valvular interstitial cells (VICs) and are lined with a monolayer of valvular endothelial cells (VECs) on the blood-contacting inflow and outflow surfaces. In developmental stages VICs synthesize the ECM. In a healthy adult state, VICs maintain a quiescent phenotype (qVICs) but may switch to activated (myofibroblast-like) VICs (aVICs) to maintain tissue homeostasis, adjust to increased stress levels, and respond to injury to modulate the ECM. The distinct layers of valve ECM facilitate their function. The layer proximal to the left ventricle, ventricularis, is rich in radially oriented elastin, providing the elasticity<sup>[54]</sup> required for extension during diastole and for recoil during systole. The layer proximal to the aorta, the fibrosa layer, consists of circumferentially aligned<sup>[55]</sup> collagen type I (70%) and III (25%),<sup>[56–58]</sup> creating tensile strengths ensuring coaptation during diastole.<sup>[59]</sup> The middle layer, spongiosa, acts as a bearing surface and impact absorbent, for it contains polar proteoglycans and glycosaminoglycans (Figure 1A).<sup>[58,60]</sup>

To withstand the repetitive hemodynamic forces of the cardiac cycle, the individual layers in the aforementioned architecture have a specific role facilitated by their ECM composition, giving them their distinct mechanical properties. The high collagen content in the fibrosa layer in its crimped and circumferential organization contributes to the anisotropic and nonlinear stress–strain response required for the load-bearing function during diastole.<sup>[61]</sup> It has been shown that the collagen bundles develop over time and that the circumferential orientation is already present in fetal valves.<sup>[62]</sup> Moreover, the number of intermolecular collagen crosslinks is responsible for the mechanical behavior in the circumferential direction, rather than the collagen quantity.<sup>[63]</sup> The stiffness of the fibrosa in the circumferential direction is significantly higher than in the radial direction, contributing to its anisotropic character.<sup>[63–65]</sup> Tissue stiffness is found to be  $\approx 2$  and 15 MPa along the radial and circumferential direction, respectively.<sup>[63]</sup> Recently, significant differences in mechanical properties of the different leaflet layers were identified by nanoindentation. The median Young's moduli were found to be 37.1, 15.4, and 26.9 kPa in the fibrosa, spongiosa, and ventricularis layer, respectively. The median Young's modulus of the intact leaflet was measured at 26.7 and 670.1 kPa in the calcified aortic valve.<sup>[66]</sup>

### 2.3. Vascular Characteristics

At the macroscopic level, (millimeter range<sup>[67]</sup>) coronary arteries present three distinct tissue layers (or tunics); intima, media, and adventitia/externa (Figure 1A). Each of these layers is characterized by specific mechanical properties, cellular populations and ECM organization.<sup>[68]</sup> The tunica intima has a thickness of  $\approx 0.3$   $\mu\text{m}$  and is formed by a monolayer of ECs longitudinally lining the inner surface of the lumen, with the main purpose being to ensure and maintain hemocompatibility, mass transport and biochemical signaling between blood and tissues.<sup>[69,70]</sup> The intima has minimal subendothelial ECM protein expression of proteoglycans and hyaluronan.<sup>[71]</sup> The tunica media is organized into repetitive medial lamellar units. The circumferential layers of elastic lamellae are

alternated with smooth muscle cells and collagen fibers with interconnecting elastin fibers.<sup>[68]</sup> The lamellar structure accommodates high blood pressures by accumulating elastic energy storage during systole and releasing it during diastole. The tunica media is predominantly composed of collagen fibers aligned in the circumferential direction. Moreover, elastin is associated with the elastic capability of the coronary arteries. Its orientation changes from slightly longitudinally aligned in the inner media to circumferentially aligned in the middle media, and to longitudinally aligned in the outer media.<sup>[72]</sup> The cellular composition of the tunica media consists mainly of mesenchymal derived smooth muscle cells. These highly specialized contracting cells exhibit an elliptic-shaped nucleus with the longitudinal axes aligned circumferentially and represent 24% of total medial volume.<sup>[73]</sup> The tunica adventitia, or externa, presents higher expression of collagen I and III than in the intima and media tunics. The collagen fibers are longitudinally aligned, which thus hinders elongation of the large vessels. Collagen I forms a rigid fibrillar structure, whereas collagen III supports vessel elastic properties. The adventitia is enclosed in an external elastic lamina that separates it from the perivascular mesenchyme. The vascular ECM is characterized by the presence of repeating assemblies of collagen into fibrils with the exception of elastin. Several studies indicate that high matrix fiber anisotropy provides strong contact guidance cues thus influencing cell orientation.<sup>[74]</sup> The cellular component of the tunica externa consists of fibroblasts aligned in the longitudinal direction.

It is known that the larger distributing arteries, such as the aorta and pulmonary artery, are rapidly and transiently distended during systole, accommodating 50% or more of the ventricular ejection volume.<sup>[75]</sup> This results in large circumferential and longitudinal strains, 23% and 25%, respectively, and circumferential and longitudinal moduli in the range of 1–6 MPa for the larger arteries.<sup>[76]</sup> The mechanism of dampening and buffering the pulsating blood flow and pressure generated during systole is accommodated by the concentric multi-layered structure and viscoelastic behavior of the vessels.<sup>[77]</sup> Mechanical properties change according to vessel diameter, location and the collagen-elastin ratio.<sup>[78]</sup> Tensile testing showed the highest maximum stress for the adventitia (1430 kPa circumferential and 1300 kPa longitudinal) and no significant difference between media and intima (ranging from 391 to 446 kPa).<sup>[79]</sup> With aging, the vascular wall becomes progressively less compliant and stiffer with a rapid progression after the age of 60.<sup>[76]</sup>

### 2.4. Fiber Scaffold Requirements

The previous sections clearly indicate that the combination of different cells together with the unique ECM structure and composition of the myocardium, valves, and vasculature is completely different and essential to ensure their distinct functionalities. From a tissue engineering (TE) approach, there are several key features that should be captured in order to ensure the TE constructs have comparable properties to their natural counterparts. These features are generally divided into structural and mechanical requirements and will differ between the three cardiac tissue components revised in the previous section.

The myocardium scaffold should typically possess an organized, elastic microfibrillar structure that could facilitate anisotropic cell organization, contraction and integration with the native tissue. A uniform honeycomb-like geometry structure has been investigated a number of times due to its favorable mechanical properties, anisotropy and deformation capabilities.<sup>[34,80]</sup> Alternatively, we envision that the combination of advanced imaging modalities like 3D Magnetic resonance imaging (MRI), biplane fluoroscopy, and intramyocardial mapping strategies with computer aided design (CAM), could be used to assess fiber organization of healthy myocardium and then translate it to a fiber formation technology to generate an electrical and mechanically compatible fiber scaffold.<sup>[50,51,53]</sup> With respect to the biomechanical properties, the fibrous scaffold should possess an anisotropic behavior and a reversible bi-axial deformation of up to 25%,<sup>[81]</sup> with a stiffness ranging from 10–20 kPa.<sup>[82]</sup> Such biomechanical environment will be particularly important to support cells and promote the formation of a mature myocardium tissue with regular beating. Since Discher's pioneer studies, it is known that stem cells, and their differentiated CMs, feel the microenvironment mechanical properties via signal transduction and change their shape and phenotype accordingly.<sup>[83–86]</sup> Another fundamental design criteria for the success of a myocardial scaffold is the integration of electroconductive properties within the fiber scaffolds material, in order to provide cardiomyocytes with proper electrical pacing, and an engineered capillary network to allow nutrient, oxygen, and waste exchange.<sup>[87]</sup>

For fiber scaffolds to mimic the native valve, fiber orientation in the radial and circumferential direction are essential to give the valves their anisotropic behavior. The collagen, elastin, and glycosaminoglycans in the trilayered leaflets give the valve its strength, pliability, and flexibility, respectively. Fiber constructs therefore must consist of three layers with a specific fiber orientation and mechanical properties to meet these requirements. Particularly, it is essential that fiber scaffolds can withstand the dynamic forces exerted on the valve during the cardiac cycle and present stiffnesses in the range of 2 MPa (radial direction) and 15 MPa (circumferential). Furthermore, the blood-contacting surfaces of the TE construct have to be smooth enough with a low friction coefficient to prevent thrombosis, coagulation, or calcification.

For vasculature replacement scaffolds, the main risks also include blood-contact complications<sup>[88]</sup> therefore the formation of a continuous endothelial monolayer is pivotal. Fiber constructs should present longitudinally-aligned fibers to guide endothelial monolayer formation mimicking the subendothelial proteoglycans and hyaluronan native ECM.<sup>[89]</sup> The addition of circumferentially-aligned fibers is also fundamental to ensure sufficient mechanical compliance to support high blood pressures, thereby mimic the native elastic alternated lamellae and collagen fibers present in the tunica media.<sup>[68]</sup> Scaffolds should allow large circumferential and longitudinal strains up to 25%, with tensile stiffnesses of  $\approx$ 1400 kPa for the adventitia and 400 kPa for both media and intima region. The pore size and pattern of the scaffold needs consideration particularly in the lumen where the construct is in contact with blood flow. There needs to be adequately large pores to allow for migration of the seeded cells, allowing them to migrate and align themselves

with the assistance of the scaffold, as well as for the integration of cells from the host at the periphery of the construct. However, this pore size should not be so large as to cause bleeding through the walls of the construct.

Additionally, the fiber scaffold bulk material has to be biodegradable and the degradation rate should be similar to the tissue remodeling speed to minimize functional deficits. Premature degradation will affect the scaffold mechanical properties and result in graft shrinkage,<sup>[90]</sup> whereas delayed biodegradation affects true tissue integration which could lead to scaffold encapsulation and scar formation.<sup>[91]</sup> Lastly, the material should not elicit an adverse immune response after implantation, as this could lead to graft rejection.

### 3. Fiber Patterning Technologies

To date, several fiber manufacturing technologies and materials have been investigated. However, there is only a subset of techniques available that can produce structured 3D fibrous scaffolds with cellular-relevant geometrical features and sizes<sup>[28,35]</sup> and with the potential to capture the aforementioned tissue-specific characteristics and design criteria. The key features, advantages and limitations of this subset of technologies is reviewed below and summarized in **Table 1**.

#### 3.1. Solution Electrospinning

Solution electrospinning (SES) is one of the most widely used spinning techniques in TE due to its capacity to produce long, nanoscale fibers, its easy setup and cost effective (**Figure 2A**). The underlying operating principle of SES consists in extruding a polymer solution through a spinneret at which point high voltage (typically between 10 and 30 kV) is applied to the spinneret, causing the polymer solution to form a Taylor cone and to accelerate toward the oppositely charged collector plate (10–15 cm collector distance).<sup>[92]</sup> As a result of the long jet travelling distances, whipping instabilities dominate the process and the fiber deposition is characteristically chaotic creating random fiber architectures.<sup>[93]</sup> Different process components have been investigated and manipulated since, thereby creating different sized fibers and scaffold architectures.

Rotating mandrels have been utilized as the collectors to achieve aligned fibers in one direction. The rotational velocity (typically above 1000 rpm) generates a tangential force, that once it exceeds the jet's velocity results in uniaxial, circumferentially aligned nanofiber collection. Nevertheless, the extent of alignment is limited to  $\approx$ 67.1% of the total volume of deposited fibers.<sup>[94]</sup> Modifications of the electrical field have also been shown to increase the level of fiber architectural control. For instance, by using parallel electrodes separated by a gap, uniaxially aligned fiber arrays can be obtained.<sup>[95]</sup> It is observed that the jet travels back and forth from one collector toward the opposite collector forming parallel fibers above the collector's gap. Through tuning the electrical charge, researchers were able to create 30 cm long and 8 cm wide aligned nanofiber arrays consisting of multiple fibers<sup>[93]</sup> and with fiber diameters smaller than 300 nm.<sup>[96]</sup> As spinning time progresses, deposited

**Table 1.** Overview of advantages and disadvantages of different fiber patterning technologies.

Fiber technology	Advantages	Disadvantages
Solution electrospinning	<ul style="list-style-type: none"> <li>• Nano to sub-micrometer scale resolution (0.01–1 μm)<sup>[93]</sup></li> <li>• Cheap</li> <li>• Easy to use</li> </ul>	<ul style="list-style-type: none"> <li>• Limited materials available</li> <li>• Limited thickness (max. 30 min of fiber deposition)<sup>[96]</sup></li> <li>• Uncontrollable and small pore size</li> <li>• Limited shape fidelity</li> <li>• Solvents (often cytotoxic) involved</li> </ul>
Melt electrospinning	<ul style="list-style-type: none"> <li>• Precise control over microarchitecture</li> <li>• Moderately thick scaffold possible (up to 7 mm)<sup>[115]</sup></li> <li>• High shape fidelity</li> <li>• Solvent free</li> </ul>	<ul style="list-style-type: none"> <li>• Limited materials available</li> <li>• High temperatures required</li> <li>• Microscale resolution (smallest = 0.8 μm)<sup>[114]</sup></li> </ul>
Near-field spinning	<ul style="list-style-type: none"> <li>• Precise control over microarchitecture</li> <li>• Nano to sub-micrometer scale resolution (0.05–6 μm)<sup>[130,134]</sup></li> <li>• Solution or melt possible</li> </ul>	<ul style="list-style-type: none"> <li>• Limited thickness (up to 100 μm)<sup>[135]</sup></li> </ul>
Rotary Jet spinning	<ul style="list-style-type: none"> <li>• Nano to sub-micrometer fiber diameters (0.05–3.5 μm)<sup>[136]</sup></li> <li>• High production rate</li> <li>• Room-temperature processing</li> <li>• Wide range of materials processing<sup>[198]</sup></li> <li>• Easy to use</li> </ul>	<ul style="list-style-type: none"> <li>• Low porosity</li> <li>• Solvents involved</li> <li>• Poor fiber placement control</li> <li>• Requires postprocessing</li> </ul>
Pull spinning	<ul style="list-style-type: none"> <li>• Ambient conditions</li> <li>• Easy to use</li> <li>• Compatible with wide range of material<sup>[141]</sup></li> <li>• Scaffold geometry control by adjusting collector<sup>[173]</sup></li> </ul>	<ul style="list-style-type: none"> <li>• Solvents involved</li> <li>• Limited fiber placement control</li> <li>• Lower throughput than rotary jet spinning<sup>[141]</sup></li> </ul>
Microfluidic spinning	<ul style="list-style-type: none"> <li>• Fibers can be tuned on morphological, structural, and chemical features</li> <li>• Direct cell deposition possible</li> </ul>	<ul style="list-style-type: none"> <li>• Slow fabrication process</li> <li>• Frequent nozzle clogging</li> </ul>

fibers onto the collector electrodes causes a build-up of charges, insulating the voltage gap and therefore distorting the jet and thus the continued accurate deposition of material. As such, multiple aligned fiber layers cannot be accurately deposited. This thickness of mesh varies across materials and is additionally affected by different processing conditions, such as changes to collector distance, humidity, voltage, needle diameter, and/or the concentration of the solution. An example of this limitation was outlined in work by Yang et al. where they reported distortion of PLA fiber alignment after 30 min of electrospinning.<sup>[97]</sup> Micropatterned collectors with various microtopographies such as sinusoidal, hexagonal and reentrant-honeycomb-shaped grooves in the range of 300–1000 μm have also been used to control 3D topography of the output scaffolds.<sup>[98]</sup> This micropatterning concept was also applied to a rotating mandrel SES system where groove- and cross-patterned tubular fiber scaffolds with inner diameters of 0.18–3.28 mm were obtained. Moreover, interconnected tubular scaffolds were fabricated by spinning onto branched mandrels.<sup>[99]</sup>

There is a large combination of polymeric materials that have been used for SES. Some of the most common used are silk,<sup>[100]</sup> poly-ε-caprolactone (PCL)<sup>[101]</sup> and poly(lactide-co-glycolide) (PLGA),<sup>[102]</sup> which are all biodegradable, and available as medical grade and FDA approved. However, both polymers have limited ability to support cell adhesion due to their hydrophobicity.<sup>[103]</sup> To overcome this, PLGA and other polymers have been bio-functionalized by incorporating cell adhesive peptides derived from laminin prior to electrospinning (N-acetyl-GYIGSRGYG (YIGSR) and arginyl-glycyl-aspartic acid (RGD)).<sup>[94]</sup> Another approach to overcome the hydrophobicity of polymers has been to coat the constructs with ECM-derived components, for example fibronectin<sup>[104]</sup> or collagen,<sup>[105]</sup> or

gelatin.<sup>[106]</sup> Blending of synthetic and natural polymers, such as collagen,<sup>[107]</sup> chitosan,<sup>[108]</sup> and alginate<sup>[109]</sup> has been also applied extensively, as this allows the synergize the material benefits of both natural and synthetic polymers. Polyurethane, a biodegradable thermoplastic elastomer, has been blended with the natural polymer, ethyl cellulose, allowing for the production of aligned, anisotropic SES scaffolds that exhibited enhancement of cardiac myoblast retention and proliferation.<sup>[110]</sup>

### 3.2. Melt Electrospinning

Melt electrospinning (MES) uses polymer melts instead of polymer solutions, eliminating the need of cytotoxic solvents, which, if not completely evaporated, will be trapped within the fabricated fiber mats.<sup>[111,112]</sup> A relatively recent developed method using melt electrospinning principles is the melt electrowriting (MEW) process. Its first appearance on TE field was reported by Brown et al. in 2011.<sup>[112]</sup> Similar to SES, an additional force (i.e., pneumatic or mechanical) is applied to the polymer melt to maintain constant polymer extrusion through the spinneret, where high voltage is applied, stimulating the formation of the Taylor cone and subsequent jet that is drawn to the oppositely-charged collector (Figure 2B). Using a computer-controlled collector platform, MEW fibers can be controllably deposited in both in-plane<sup>[34]</sup> and out-of-plane directions.<sup>[113]</sup> Although fiber diameters obtained by MEW are typically in the micrometer scale, Hochleitner et al. reported on the fabrication of organized fiber scaffolds with fiber diameters of ≈800 nm.<sup>[114]</sup> Moreover, fabrication of scaffolds with thickness up to a few millimeters is possible (typically <3 mm).<sup>[112]</sup> However, as the scaffold layers increase, residual charges on

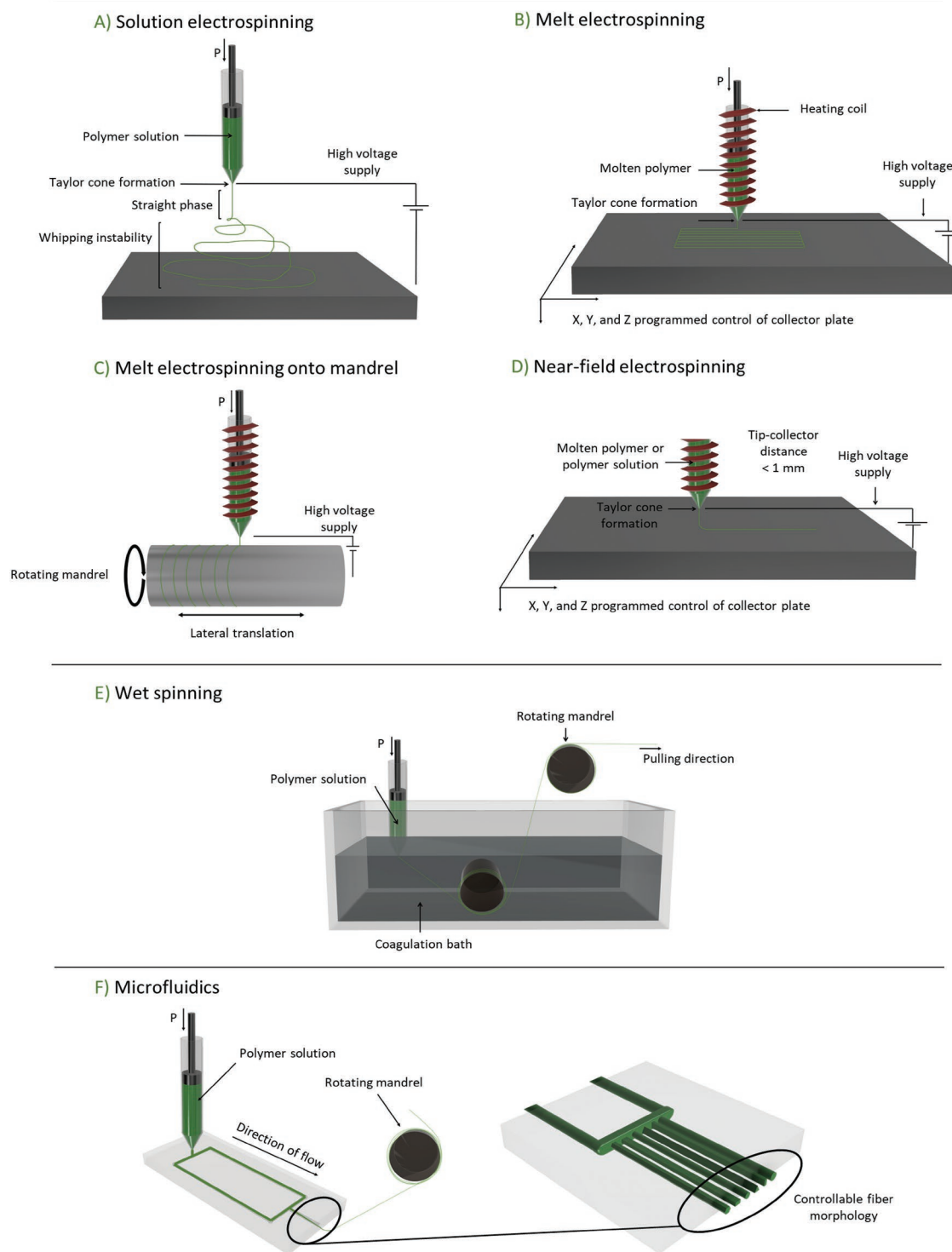


**Figure 2.** Schematic representations of key fiber manufacturing technologies with which ordered fibrous scaffolds can be obtained. A) solution electrospinning, B) melt electrospinning basic principle with extension to demonstrate the use of a C) rotating mandrel, D) near-field electrospinning, E) wet-spinning, and F) microfluidic spinning.

the previously deposited fibers increase causing instabilities in fiber deposition. To overcome this, Wunner et al. developed a mechatronic system that adjusts the collector distance during

the printing process based on the build height of the scaffold. In-process simulation of the applied voltage maintains electrostatic forces, allowing fabrication of thicker scaffolds



up to 7 mm.<sup>[115]</sup> The left ventricle myocardial thickness ranges from 4.4 to 7.4 mm at the mid-cavity level,<sup>[116]</sup> translating that this recent advance in MEW technology makes it possible to obtain anatomically-relevant thick microfiber scaffolds for myocardial TE with controllable microarchitectures.

A multitude of fiber scaffold microarchitectures with high shape fidelities have obtained to date using MEW. Squared,<sup>[28]</sup> rectangular<sup>[117]</sup> and hexagonal architectures<sup>[34]</sup> have been fabricated with pore sizes ranging from 150 to 1000  $\mu\text{m}$ . Moreover, MEW of serpentine microarchitectures with 0.5–1 mm pore sizes could also be obtained by optimizing collector speed (280  $\text{mm min}^{-1}$ ), voltage (6–6.5 kV), and pressure (2 bar) printing parameters.<sup>[118]</sup> Control over inter fiber distances is critical to allow cardiac cells growth and proliferation. Typically, epithelial and myocardial cells are in the range of 8–12  $\mu\text{m}$  and 10–100  $\mu\text{m}$  respectively,<sup>[87]</sup> and therefore pore sizes must not be smaller than that. Scaffolds characteristics of these required dimensions could be obtained with MEW, as the fiber diameters that can be deposited are 5–40  $\mu\text{m}$  and minimal interfiber distances of 90–150  $\mu\text{m}$ .<sup>[111,114]</sup> Researchers have also showed the possibility of melt electro-writing onto rotating mandrels to fabricate tubular fiber scaffolds with controlled microarchitectures (Figure 2C). With this approach, the collector speed is a combination of the rotational and translation speeds and by manipulating these two factors, varied scaffold pore morphologies can be obtained.<sup>[119]</sup> To date, tubes with inner diameters of 1.5 mm, pore sizes >1 mm, 200  $\mu\text{m}$  scaffold thickness and a variety of rhombic shaped boxes have been obtained.<sup>[120]</sup>

Presently, only a fraction of commercially available polymers are suitable to be processed using MEW due to the very specific process requirements, mostly high thermal stability (melt heating 60–350  $^{\circ}\text{C}$ ), low electrical conductivity ( $10^{-6}$ – $10^{-8}$   $\text{S m}^{-1}$ ) and high molecular weights (>12 000  $\text{g mol}^{-1}$ , but  $\leq 190\,000$   $\text{g mol}^{-1}$ ).<sup>[121]</sup> In recent years, more polymers have shown compatibility with MEW including mostly thermoplastics such as PCL,<sup>[34]</sup> polypropylene,<sup>[122]</sup> polyethylene,<sup>[123]</sup> poly(methyl methacrylate),<sup>[124]</sup> and poly(2-ethyl-2-oxazoline) (PEtOx).<sup>[125]</sup> The thermoplastic elastomer, poly(urea-siloxane), has also been investigated as a material of interest due to its processability and compatibility with MEW, with some aspects including smooth-surfaced fibers superseding PCL. Moreover, the study obtained 360  $\mu\text{m}$  thick square scaffolds with scaffold pores of 1 mm.<sup>[126]</sup> However, most of these are hydrophobic, exhibit slow degradation rates and have poor conductivity, which would be desirable characteristics of candidate materials for cTE applications. Therefore, polymer composites have been developed to improve biological compatibility by increasing the hydrophilic nature, for example, a hydroxyl-functionalized polyester, poly(hydroxymethylglycolide-co- $\epsilon$ -caprolactone) (pHMGCL), was recently proposed showing improved cardiac progenitor cell alignment compared to PCL.<sup>[117]</sup>

### 3.3. Near-Field Electrospinning

Near-field electrospinning (NFES) utilizes smaller collection distances (0.5–1 mm) and lower acceleration voltages (0.2–5 kV) than SES or MES to allow for controllable fiber deposition.<sup>[127]</sup> The use of a lower voltage increases the range of materials that

can be used<sup>[128]</sup> and increases the deposition substrate variety (Figure 2D). A lower voltage would normally reduce the fiber diameter,<sup>[129]</sup> however, the reduced tip-to-collector distance counteracts this reduction in fiber diameter. Furthermore, NFES have been reported with both molten polymers<sup>[114,130]</sup> and polymer solutions.<sup>[131,132]</sup> Melt and solution NFES share similar advantages and disadvantages as solution and melt spinning; solution NFES allows for smaller diameter fiber deposition but includes toxic solvents. Compared to traditional electrospinning however, solution NFES exhibits less fiber thinning as the flight phase is shorter. Therefore, fiber diameters that can be obtained by NFES are higher than traditional electrospinning, typically in the range of 0.05–30  $\mu\text{m}$  as opposed to 0.01–1  $\mu\text{m}$ .<sup>[133]</sup> Whereas reasonably ordered structures can be achieved by this approach, the amount of layers that can be deposited without fibers distortion is limited due to charge accumulating effects.<sup>[134]</sup> The thickest scaffolds that could be obtained contained 20 layers, and were 100  $\mu\text{m}$  thick.<sup>[135]</sup>

Recently researchers have been able to decrease the applied voltage from the typical NFES voltage (2–12 kV) to 50 V while still being able to spin a variety of materials with fiber placement control.<sup>[128]</sup> They were able to deposit squared boxes, straight lines, and curly lines with interfiber distances of  $\approx 100$   $\mu\text{m}$ . Moreover, they showed that deposition was possible on substrates that are conducting (silicon), insulating (glass), on hydrogels and on solid substrates. Additionally, deposition of a thermoplastic (polystyrene), a water soluble polymer (polyvinylpyrrolidone), a hydrophilic polymer (poly(ethylene oxide)), and gelatin was all possible.<sup>[128]</sup>

### 3.4. Solution Spinning

Rotary Jet Spinning (RJS) is a form of solution spinning that is able to produce highly aligned nanofibers. RJS uses a high-speed rotating polymer reservoir to propel a polymer solution through the spinneret by the effect of a centrifugal force. This force determines the resulting fiber diameter; the higher the centrifugal force, the thinner the deposited fiber. Additionally, the more volatile the solvent, the thicker the fiber, as rapid solvent evaporating results in rapid polymer solidification.<sup>[136]</sup> RJS typically deposits fibers with nanometric sizes. The centrifugal forces allow the collection of aligned fibers along the surface of the collector drum. This process presents different advantages over SES as it is not dependent on the polymer solution's conductivity for constant fiber deposition and typically has faster fiber deposition rates.<sup>[137]</sup>

RJS has been proven for the processing of natural polymers, like collagen, producing mechanically stable and insoluble collagen fibers due to the fibrillogenesis induced by the centrifugal forces.<sup>[138]</sup> Moreover, RJS has shown additionally superior protein-polymer hybrid applications compared to standard spinning process. In a study that compared protein surface content of 75/25-PCL/collagen blends produced with RJS and with electrospinning, greater protein content on the surface of the RJS produced fibers were found.<sup>[137]</sup> This demonstrated that RJS-produced scaffolds can have enhanced cytocompatibility, as the proteins have a higher bioavailability. In fact, scaffold compatibility with CMs in terms of sarcomerogenesis was

recently demonstrated on RJS scaffolds.<sup>[137]</sup> Recently, Dotivala et al. adjusted the RJS technique through using a rotating collector that can be manipulated in regards to orientation. Fiber layers with interspaced 90°, 45°, and 30° orientation and a constant interfiber distances of 250 μm could be deposited.<sup>[139]</sup> Although promising, fiber diameters were larger than 100 μm and only 2 layers were reported.

Blow spinning is a solution spinning technique recently reported. It uses a concenteric syringe in which the polymer solution is pressed into the inside of the nozzle and a gas on the outside at high pressures. This results in a polymer solution flight and solution evaporation during it. Aligned fibers can be obtained if the polymer is collected onto a rotating mandrel. The polylactic acid fibers have same small diameters as in SES (nanometer range), but the production time is significantly increased.<sup>[140]</sup> Moreover, although not mentioned by the authors, it is expected that more stable aligned layers can be obtain onto a rotating mandrel, as no electric field distortion will be involved.

An additional solution spinning technique of interest is pull spinning, which works by injecting a polymer solution through a needle to the high-speed rotating bristle, which then pulls and projects the polymer into parallelly-aligned fibers collected on a rotating mandrel. It has been demonstrated to produce aligned nanofibers of both natural (i.e., gelatin Type A) and synthetic polymers (i.e., PCL) using a simple setup and fast production rates for thin muscular films for smooth and skeletal muscle TE.<sup>[141]</sup>

### 3.5. Wet Spinning

Among the different fiber formation methods, wet-spinning methods have the longest history. The process is based on extruding a prepolymer into a coagulation bath to polymerize the solution into a fiber<sup>[142]</sup> (Figure 2E). Recently, a computer-assisted system has been integrated with the wet-spinning process to produce 3D scaffolds.<sup>[143]</sup> The computer-assisted system can move the needle in the in- and out-of-plane directions and the collector with coagulation bath up and down, thereby allowing for controlled layer-by-layer fiber deposition. Due to the triaxial control, scaffold patterns in any preferred form can be achieved. Moreover, because polymerization occurs in a fluid bath, the fabrication process leaves room production of overhanging structures that cannot be fabricated with conventional, open-air, 3D printing. Dini et al. fabricated PCL scaffolds of 4 × 20 × 3 mm that could be used for bone TE as it is a clinically relevant size.<sup>[144]</sup> However, with this approach, fiber diameters are typically above 200 μm, as the fiber diameter is limited by the depositing inner needle diameter.<sup>[145]</sup> To obtain smaller diameters, researchers have applied a mechanical stretching principle using a rotating mandrel to create fibers with diameters in the range of 20–600 μm.<sup>[146,147]</sup> Qiu et al. utilized ceramic capillaries with inner diameters of 28 μm in the place of a needle in combination with postspinning mechanical stretch allowing for silk-elastin-like protein copolymer fibers of less than 10 μm.<sup>[148]</sup> Additionally, the rotating mandrel induces a circular flow within the coagulation bath, so once the prepolymer solution is injected within the coagulation

bath it experiences shear forces. These shear forces can be used and tuned by adapting the polymer composition and flow rate to obtain fiber mats with aligned fibers.<sup>[146]</sup> Nevertheless, the microarchitectural control is limited, since only parallelly-aligned scaffolds can be obtained onto the rotating collector mandrel. Wet-spinning has used a large variety of materials including alginate,<sup>[146,147]</sup> chitosan,<sup>[149]</sup> poly(L-lactic acid) (PLLA)/chitosan blends,<sup>[150]</sup> or PCL.<sup>[145]</sup> A converged approach, electro-wet-spinning combines the properties of wet spinning and electrospinning in order to further minimize fiber diameter, as demonstrated using poly(chitosan-g-dl-lactic acid).<sup>[151]</sup>

### 3.6. Microfluidic Spinning

Microfluidic spinning (MS) converges the principles of micro-scale fluid dynamics and wet spinning. The process was developed more than 10 years ago after the introduction of the microfluidics technology.<sup>[152]</sup> It is based on the combination of a coaxial laminar flow on a microfluidic chip in which a prepolymer and a crosslinking reagent meet right before extrusion (Figure 2F). The crosslinking mechanism can be initiated through photo polymerization<sup>[153]</sup> or via chemical reactions.<sup>[154,155]</sup> Fiber diameters ranging from nanometer range<sup>[154]</sup> to several hundred micrometers<sup>[156]</sup> with uniform diameters can be fabricated successfully without complicated spinning setups and collectors.<sup>[157]</sup> Additionally, MS has a great potential to directly incorporate cells within the polymer fibers as the cells are only shortly exposed to a high shear stress due to the short microfluidic channel distances, and no other hazardous factors, such as heat and solvents.<sup>[142]</sup> Through adaptation of the microfluidic platform, fibers with various shapes and patterns can be obtained (Figure 2F). Next to solid fibers,<sup>[153]</sup> fibers with grooves,<sup>[158]</sup> with a lumen,<sup>[159]</sup> flat,<sup>[160]</sup> and hybrid fibers<sup>[158]</sup> can be fabricated by adjusting the microfluidic lumen design.<sup>[161]</sup> Typically, control over fiber alignment can be obtained by using a rotating collector glass.<sup>[162]</sup> Mosaic hydrogel scaffolds consisting of complex patterns and built up from a multitude of different materials have been obtained by using multiple-channel microfluidic chips. It was demonstrated by Leng et al. that fiber scaffolds with a mosaic-like shape can be fabricated by extruding uncrosslinked fluids into a channel network that deposit crosslinked material in the desired pattern. The authors fabricated 150–350 μm thick flat and tubular scaffolds with a variety of patterns, such as arrays of voids, patterned spots, and parallel stripes of distinct materials.<sup>[163]</sup>

Generally, materials used for microfluidic spinning need to be polymer solutions that can be crosslinked using photo or chemical crosslinking methods and materials that have a viscosity that allows for a constant laminar flow. Various natural polymers including alginate,<sup>[159]</sup> collagen and chitosan<sup>[164]</sup> have been explored and showed compatibility with microfluidic spinning. Synthetic materials have also been processed and spun into fibers using microfluidic spinning. These include PLGA,<sup>[162]</sup> polyurethane (PU),<sup>[165]</sup> polyurethane acrylate,<sup>[153]</sup> and 4-hydroxybutyl acrylate.<sup>[152]</sup> The most frequently used material is alginate, due to quick and reproducible crosslinking process.<sup>[166]</sup>

**Table 2.** Summary of existing fiber patterning technologies for cTE with resultant scaffolds and their respective properties. Symbols: NE: not evaluated.

Fiber technology	Architecture	Fiber diameter	Pore size / Porosity	Mechanical properties	Application	Ref.
Solution electrospinning	Aligned	269 ± 33 nm	≈1.5 μm	1.45 ± 0.20 MPa Young's Modulus, 0.17 ± 0.05 MPa tensile strength	Myocardium	[168]
Solution electrospinning	Aligned	≈2.5 μm	≈2 μm	87.9 ± 24.7 MPa Young's Modulus	Myocardium	[169]
Solution electrospinning	Aligned	1.53 ± 0.05 μm to 5.13 ± 0.19 μm	480 ± 85 μm <sup>2</sup> to 980 ± 150 μm <sup>2</sup>	1.22 ± 0.07 MPa Young's Modulus	Myocardium	[171]
Solution electrospinning	Aligned	Nanorange	Microporosity	500 ± 31 kPa longitudinal tensile elastic modulus, 74 ± 15 kPa transverse tensile elastic modulus	Myocardium	[173]
Rotary jet spinning	Aligned	≈425 nm	NE	≈17.5 ± 6.6 MPa Young's Modulus	Myocardium	[136]
Solution electrospinning	Aligned tube	4.04 ± 0.25 μm	Porosity: 78–81%	3 MPa radial tangent modulus, 4.1 MPa circumferential tangent modulus	Valves	[181]
Solution electrospinning	Trilayered tubular	≈150–500 nm	NE, porous middle layer	Aligned parallel: 23.03 ± 2.00 MPa, aligned perpendicular: 5.26 ± 0.31 MPa, random 15,73 ± 2.55 MPa	Vasculature	[185]
Melt electrospinning	Squared and rectangular	4–12 μm	150–300 μm	0.70 ± 0.15 to 2.05 ± 0.15 MPa tensile modulus	Myocardium	[117]
Melt electrospinning	Hexagonal	NE	250–800 μm	5–11 MPa modulus in x-direction; 1–2 MPa modulus in y-direction	Myocardium	[34]
Melt electrospinning	Serpentine shaped	19.76 ± 1.54 μm	250 μm to 1 mm	3.07 ± 0.23 to 4.87 ± 0.094 MPa tensile modulus	Valves	[118]
Near-field electrospinning	Aligned fibers	0.5–3 μm	5–100 μm	NE	Vasculature	[128]
Wet spinning	Aligned tubular	NE	1–5 μm	NE	Vasculature	[186]
Microfluidic spinning	Mosaic fibers, aligned tubular scaffolds	≈50 μm, 1.5 mm tube diameter	NE	NE	Myocardium, vasculature	[163]
Microfluidic spinning/textile technology	Hallow and solid fibers, weaved scaffolds with rectangular pores	20 ± 14 μm to 210 ± 5 μm	≈ 200 × 1000 μm	6.3 ± 0.4 Pa to 730 ± 15 Pa Youngs modulus measured by an atomic force microscope across three different materials	Myocardium, vasculature	[159]

## 4. Applications of Patterned Fiber Scaffolds in cTE

The following section will set out how current microfiber scaffolds are used and combined with cells for cTE. Key examples for the myocardium, the cardiac valves and vasculature will be discussed below and summarized in **Table 2**.

### 4.1. Myocardium

A number of different fiber formation techniques have been used to fabricate scaffolds for myocardium recapitulation and/or repair, including SES, RJS, pull spinning, and MEW.

SES has been utilized to obtain nanofiber scaffolds, where researchers co-electrospun fibrin and PLGA, in randomly oriented fiber scaffolds with fiber thicknesses ranging from 50–300 nm and 2–4 μm, respectively. The PLGA/fibrin scaffolds showed higher efficacy for CM differentiation from umbilical cord blood-derived mesenchymal stem cells than PLGA alone, as indicated by cardiac differentiation marker expression (i.e., α-sarcomeric actinin and troponin). While the construct allowed for sufficient cellular infiltration, the random alignment of the fibers resulted in no evidence of cellular anisotropy as in the

native tissue. Nevertheless, the combination of fibrin and PLGA fibers was beneficial as fibrin naturally degraded after 3 weeks in culture, allowing sufficient time for collagen produced by the cells to replace it, while PLGA remained throughout for mechanical support.<sup>[102]</sup> To obtain fiber alignment and anisotropy similar to native myocardium tissue, SES constructs have further been manipulated either during or after production with heat and mechanical forces to create parallelly-aligned microfiber scaffolds (**Figure 3A,B**). These SES scaffolds enabled iPSC-derived CMs and ECs to align better and show signs of maturation (**Figure 3C**). Compared to the random pattern, sarcomere lengths became significantly larger in the aligned scaffolds. Moreover, contraction velocity upon electrical stimulation of CMs was significantly higher in the aligned SES scaffolds than in the random SES scaffolds. Consequently, an aligned SES scaffold pattern was better able to support iPSCs-CMs than a random pattern.<sup>[167]</sup>

Using SES with a rotating mandrel as the collector, Kai et al. obtained aligned PCL/gelatin nanofiber scaffolds and found similar results in that seeded CMs had an enhanced degree of cellular alignment and orientation in the aligned scaffolds versus random scaffolds.<sup>[168]</sup> Khan et al. used the same technique to obtain highly aligned PLGA nanofiber scaffolds which

showed positive effects of hiPSC-CM alignment. It was seen that hiPSC-CMs had upregulated maturation gene expression, including troponin-T and  $\alpha$ -actinin, as well as enhanced calcium cycling when cultured on the aligned PLGA scaffold than when cultured on a conventional flat culture plate.<sup>[169]</sup> Hsiao et al. obtained aligned composite fibers (polyaniline and PLGA) that were further transformed into a conductive material by doping into HCl. After 3 days in culture, the conductive scaffolds showed synchronous beating of CM clusters upon electrical stimulation whereas the undoped, less conductive scaffolds remained unsynchronized. This study demonstrated the importance of scaffold conductivity for synchronized CM beating and electrical integration for implantation.<sup>[170]</sup> Lastly, Fleischer et al. obtained aligned SES fiber scaffolds using globular serum albumin, as albumin has beneficial mechanical (elasticity and higher strength than other biomolecules), biochemical (hydrophobic cavities), and biodegradable characteristics, making it a promising material for cTE. Albumin was made compatible with SES by adding trifluoroethanol, as this unfolds the albumin and allows its processing.<sup>[171]</sup>

RJS has been used to fabricate aligned micrometer-scaled fibers of various compositions of PCL and PCL blended with collagen and gelatin.<sup>[137]</sup> The aligned PCL fibers promoted sarcomere formation in 20% of CMs and the aligned PCL/collagen blends in 80% of CMs following 5 days in culture. As sarcomere generation is a vital aspect for its contractile function, PCL/collagen blend aligned fiber scaffolds show promises for cardiac patch engineering. It was additionally suggested by the authors that PCL may have some protective effect on the collagen, which would have typically become denatured as a cause of the fluoroalcohol solvent used.<sup>[137,172]</sup> A more recent study utilized the process of pull spinning for the fabrication of a ventricle-like nanofiber scaffold. Researchers designed a ventricle-shaped (ellipsoidal) mandrel to collect PCL-gelatin nanofibers in an anisotropic pattern with the size of a rat ventricle (Figure 3H). Following 14 days in culture, cells and sarcomeric alignment was seen along the direction of the nanofibers (Figure 3I). The scaffold design could both support rat CMs and iPSC-CMs, highlighting the suitability of this strategy to translate to a human model. Regarding the mechanical suitability of the construct produced using pull spinning, it was found that it had a higher tensile elastic modulus than the ECM of native myocardial tissue ( $E \approx 500$  kPa and  $\approx 350$  kPa, respectively).<sup>[173]</sup> This factor could be further refined to match the ventricular mechanics of the patient species through changing the material, scaffold degradation rate and tuning of the pull spinning protocol.

Recently, MEW scaffolds of PCL were seeded with CPCs in rectangular ( $150 \mu\text{m} \times 300 \mu\text{m}$ ) microstructures. CPCs aligned along the rectangular long size, whereas no anisotropic alignment was observed in a squared microstructure scaffold.<sup>[117]</sup> Interestingly, cells located far (up to  $150 \mu\text{m}$ ) from the fibers appeared to align accordingly, indicating that a fiber architecture an order of magnitude larger than the native ECM can already promote cellular organization.<sup>[117]</sup> One major disadvantage of these scaffolds is the limited elastic deformation, 2–3.5%, that did not approximate the native myocardium deformation. Recent research efforts have looked into alternative microarchitectures to improve scaffold deformation.

Sinusoidal fiber morphologies have been shown to allow a notable elastic tensile strain of 45%.<sup>[174]</sup> Additionally, hexagonal micro architectures of 400–800  $\mu\text{m}$  side lengths were reported<sup>[34]</sup> that exhibited large biaxial deformations, up to 40% strain, and approximates the native myocardium hexagonal-like microarchitecture (Figure 3D,E).<sup>[80]</sup> Importantly, the hexagonal MEW-produced scaffolds possess shape memory that allows noninvasive cardiac delivery to the heart through a catheter as demonstrated in a porcine model. From a CMs maturation point of view, it was seen that the hexagonal architecture enhanced a mature gene expression pattern compared to the rectangular-pattern scaffolds, including the expression of electrical coupling gene connexin 43, alpha cardiac actin, calcium handling gene SERCA2a and mitochondrial gene TOMM70. Additionally, there was an increase in sarcomere length, cellular alignment (Figure 3F,G) and contraction rates which are all indicators of CMs maturation. Although these approaches showed promising results for architectural, mechanical and cellular characteristics, reparative integration and functional coupling to the native myocardium is only superficially studied and warrant further explorations.

#### 4.2. Cardiac Valves

Fibrous scaffolds have been extensively used for cardiac valve TE. Fiber formation techniques that have been used are textile weaving technology, SES, and MEW. Through the use of textile weaving technology, Hoerstrup et al. developed a trileaflet shape by combining nonwoven PGA fibrous meshes coated with poly-4-hydroxybutyrate (P4HB).<sup>[90]</sup> The trileaflet constructs were seeded with myofibroblasts and ECs, and matured for 28 days in a bioreactor under dynamic flow before evaluation in a ovine model. 8 weeks postimplantation the fibrous graft was degraded, and 20 weeks post implantation ECM constituents were comparable to the native pulmonary valve. The researchers showed graft functionality up to 5 months, however, long-term functionality was not evaluated.

A combination of SES and textile weaving technology was employed to fabricate woven of yarns of polyacrylonitrile with a  $250 \mu\text{m}$  thickness. This scaffold was then embedded within a hydrogel to increase the mechanical properties and to allow uniform embedding of VICs. The scaffold recapitulated the circumferential anisotropy and the radial nanofiber direction similar to native aortic valve. Moreover, the VICs on the composite material displayed a healthy fibroblast-like phenotype, whereas VICs only embedded in the hydrogel constructs showed increased pathological osteoblast-specific gene expression.<sup>[175]</sup> Using SES, Masoumi et al. created a cardiac valve with an aligned but anisotropic fiber orientation by depositing P4HB fibers on top of a rotating mandrel.<sup>[176]</sup> The obtained aligned fiber microstructure had a fiber diameter of  $1.8 \mu\text{m}$  and an elastic modulus similar to that of valve leaflets. Wu et al. fabricated an anisotropic scaffold with mechanical properties similar to the native aortic valve (Section 2.2). Nevertheless, trileaflet architecture could not be recapitulated in either study. Interestingly, Moreira et al. created a functional trileaflet valve with partly organized fiber organization. Multi-fiber Poly(L/DL)-lactide (PLDL) bundles were circumferentially

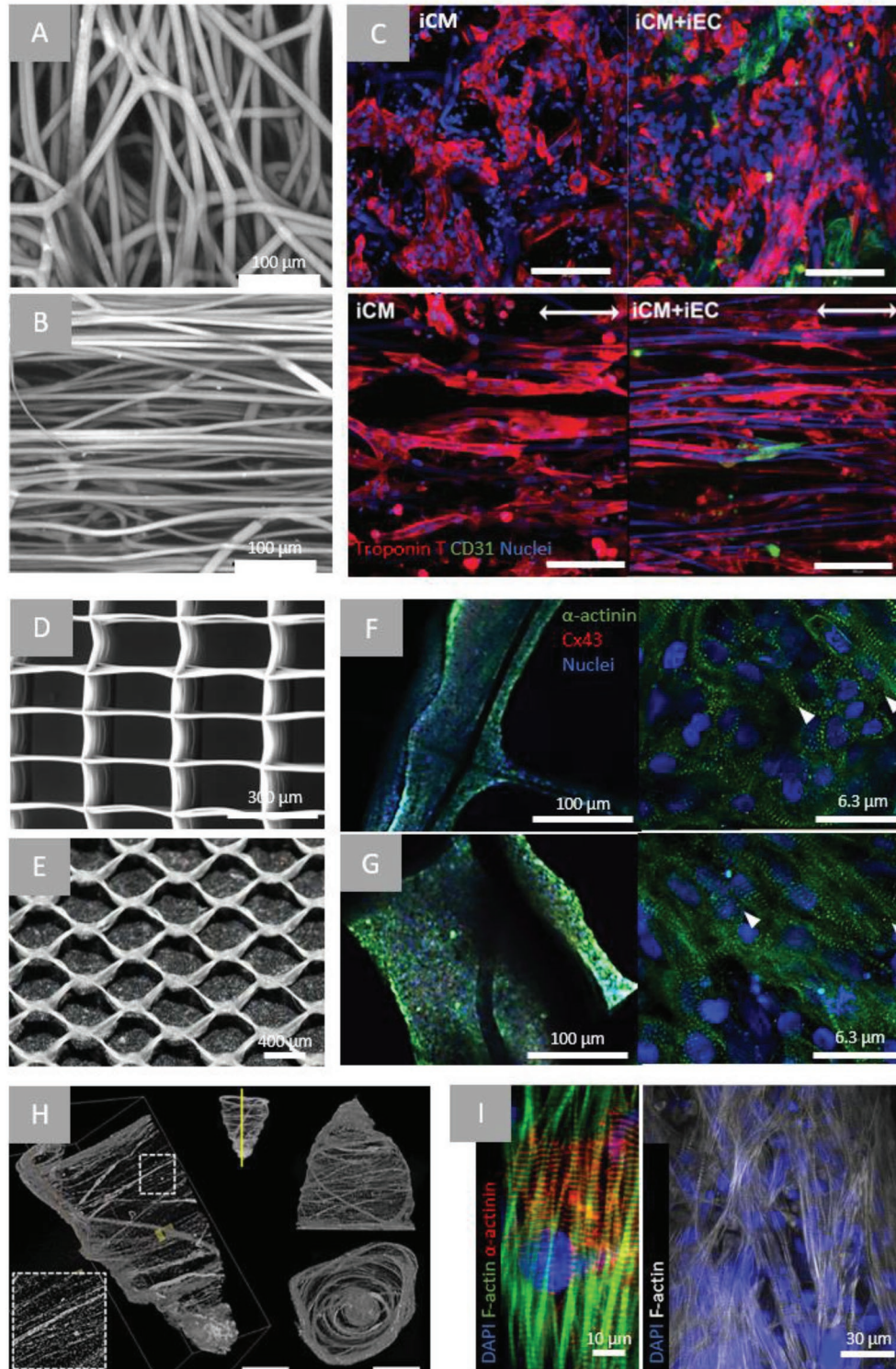


**Figure 3.** Examples of microfiber scaffolds applied for myocardial TE approaches. A) confocal microscopy images of PCL electrospun mesh with randomly oriented fibers and B) aligned fibers following heat and mechanical manipulation, C) confocal microscopy of iPSC-CMs (troponin T—red) and/or iPSC-ECs (CD31—green) after 48 h of culture on random or aligned PCL electrospun scaffolds (scale bar = 100  $\mu\text{m}$ ). Arrow indicating direction of fiber alignment. Reproduced with permission. Copyright<sup>[167]</sup> 2017, The Royal Society of Chemistry). D) SEM images of PCL scaffold fabricated using MEW of rectangular (150  $\times$  300  $\mu\text{m}$ )<sup>[17]</sup> and E) hexagonal pattern (hexagon side length = 400  $\mu\text{m}$ ), confocal microscopy images of  $\alpha$ -actinin (green), nuclei (blue) and connexin-43 (red) staining of iPSC-CMs in rectangular (F) and hexagonal (G) scaffolds.<sup>[34]</sup> H)  $\mu\text{CT}$  of pull-spun rat ventricle scaffold (scale bars: left = 10 mm, right = 5 mm), I) immunofluorescent stainings (as indicated) of iPSC-CMs cultured in scaffolds for 14 days. Reproduced with permission.<sup>[173]</sup> Copyright 2018, Springer Nature.

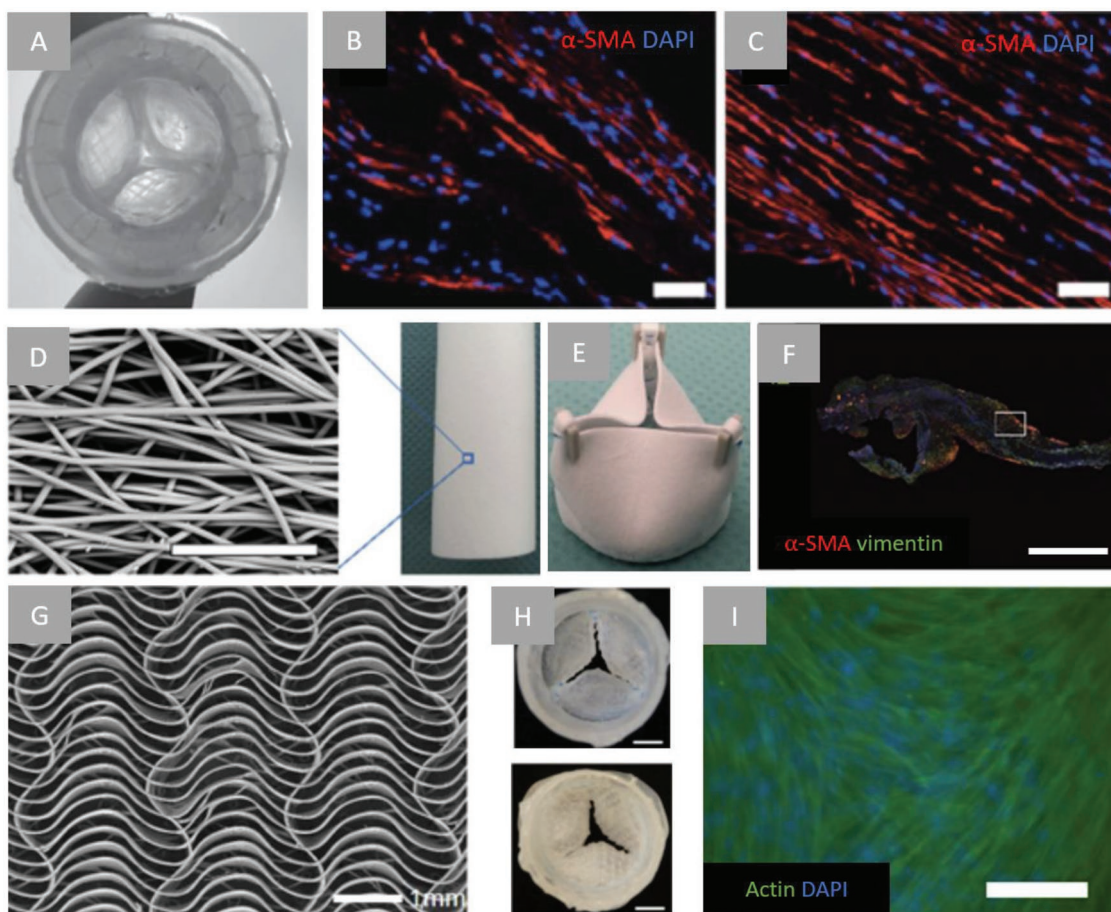


**Figure 4.** Examples of fibrous scaffolds applied on cardiac valve engineering. A) aortic view of textile-fibrin composite scaffold (valve diameter = 1.8 cm), B)  $\alpha$ -SMA immunofluorescent staining of textile-fibrin composite scaffold leaflet and wall, C) Aligned actin fiber presence along longitudinal direction after dynamic culture (scale bar = 50  $\mu$ m). Reproduced with permission.<sup>[177]</sup> Copyright 2016, Wiley-VCH. D) SEM of close up electrospun tubular scaffold (scale bar = 50  $\mu$ m) and E) sutured scaffold into a valve, F) longitudinally cut part of transections of valve leaflets that were implanted in sheep for 12 months shows cellular infiltration and cells expressed  $\alpha$ -SMA (red) and vimentin (green) (scale bar = 1 mm). Reproduced with permission.<sup>[181]</sup> Copyright 2017, Elsevier. G) SEM image of MEW fabricated serpentine architecture fibrous scaffold, 20 layers, 0.25 mm circumferential and 2 mm radial pore size, and H) MEW scaffold sutured as cardiac valve, aortic view (top) and ventricular view (bottom) (scale bar = 5 mm), I) immunofluorescent analysis of fibrin/HUVMC-embedded MEW scaffolds 2 weeks in culture (scale bar = 200  $\mu$ m). Reproduced with permission.<sup>[118]</sup> Copyright 2019, Wiley-VCH.

placed into a frame and were attached using electrospinning of PLGA fibers on top (Figure 4A). The construct was molded into a trileaflet shape and embedded within vascular cells loaded fibrin gel and matured under increasing dynamic conditions. The composite scaffold was functional under the physiological forces and showed ECM remodeling. Although no in vivo evaluation was carried out, this approach shows promise for in vivo functionality.<sup>[177]</sup>

A recent study using MEW showed the fabrication of a trileaflet valve compatible with aortic valve pressures. Saidy et al. fabricated a PCL scaffold with viscoelastic properties similar to native valves. This was achieved by producing a valve scaffold composed of sinusoidal fibers placed in the radial and circumferential direction (see Figure 4G–I). Human vascular smooth muscle cells could grow on the scaffold once encapsulated in fibrin gel. Three single MEW leaflets with cell-laden fibrin gel were sutured on a silicone mold mimicking the aortic root to obtain a functional trileaflet valve (Figure 4H).<sup>[118]</sup>

All aforementioned preformed cell-laden scaffolds were cultured in vitro to generate an implantable, nonimmunogenic graft allowing for integration postimplantation. Additionally, they all require in vitro maturation in a bioreactor to obtain sufficient mechanical strength to withstand hemodynamic forces to be a candidate for in vivo work. Nevertheless, for clinical translation a scaffold with greater a-priori mechanical compatibility could be desirable. However, strict regulations, in vitro culture requirements, and logistics prevent off-the-shelf availability.

Decellularized tissue-engineered heart valves or cell-free heart valves scaffolds for growing a heart valve in situ after implantation are promising solutions. The former exhibit better anisotropy, biocompatibility, adhesion, and remodeling, though have limited scalability, require a patient-compatible cell source, are more time consuming to produce, and require complex and costly bioreactors for preconditioning. Promising results have been achieved in ovine<sup>[178]</sup> and nonhuman primate<sup>[179]</sup> studies. The latter approach does not require in

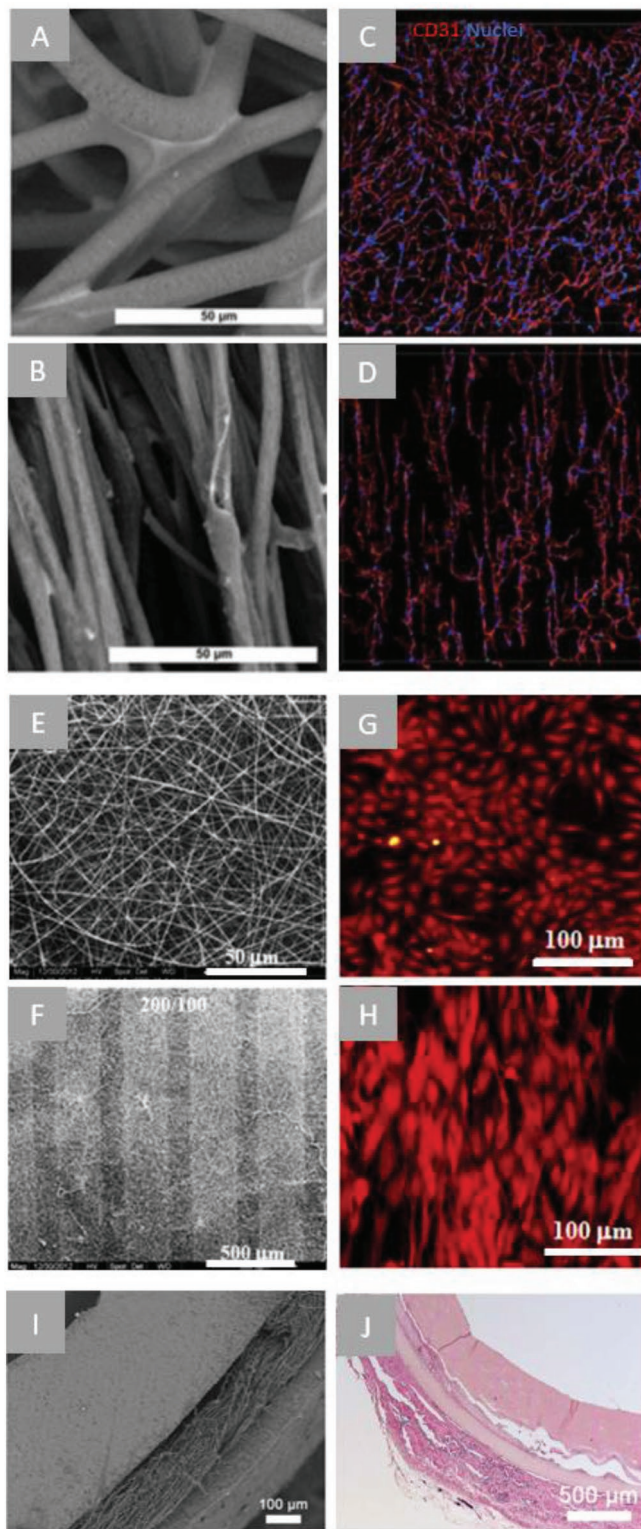


**Figure 5.** Examples of fibrous scaffolds applied on the vascular engineering. A) SEM images of a random, B) and aligned electrospun scaffold (scale bar = 50  $\mu\text{m}$ ), C) CD31 staining (red) and DAPI staining (blue) generated configurations of iPSC derived endothelial cells on a randomly oriented scaffold and D) an aligned electrospun scaffold. Scale bars not stated in original paper. Reproduced with permission. Copyright<sup>[182]</sup> 2017, Springer Science+Business Media. E) SEM pictures of a random electrospun fibrous

vitro culture, is easily available and produced due to synthetic biocompatible anisotropic fibers with tunable mechanical properties, and is consequently faster and less immunogenic. However, the quality and functioning of in situ TEHV depend on the regenerative capacity of the host, and require fine-tuning of the degradation of the biomaterials versus the regeneration of the tissue without compromising valve function.<sup>[180]</sup> Stability and functionality, 6 and 12 months after implantation of a SES bioresorbable supramolecular bis-urea-modified polycarbonate-based in situ TEHV (Figure 4D–F) in an ovine model were excellent, and pathological calcification was absent.<sup>[181]</sup>

### 4.3. Vasculature

Vascular TE has also used fiber formation techniques to generate scaffolds that mimic structure and function of native vasculature. For this cardiac tissue, SES, wet-spinning and textile technologies have been mostly used. Kim et al. seeded iPSC-derived ECs in SES PCL/polyethylene oxide (PEO) fibrous scaffolds which were 800  $\mu\text{m}$  thick with randomly oriented or parallel-aligned fiber morphologies (Figure 5A,B). The cells aligned with the parallel-aligned fiber direction (Figure 5D) and as a result, ECs seeded presented higher endothelial phenotypic markers including CD31 and CD144, and significantly upregulated endothelial nitric oxide synthase transcription. The aligned scaffolds caused the cells to assemble significantly longer vessel-like networks compared to randomly aligned fibers. Thus topographical patterning can also induce vascular network organization and maturation.<sup>[182]</sup> Deepthi et al. also used SES, but they obtained a trilayer scaffold mimicking the fiber orientation and mechanical properties of a vascular network. They spun a mixture of poly(hydroxy butyrate-co-hydroxy valerate) (PHBV) and poly(vinyl alcohol) (PVA) for the intima layer and PHBV and elastin for the tunica media and adventitia. The PHBV fibers produced were in the range of 500–800 nm and matched the native ECM structure through careful manipulation of the printing parameters. The vascular-mimicking scaffold showed hemocompatibility and induced HUVEC and smooth muscle cells alignment, and elongation according to the layer-specific fibers direction. The increasing radial-oriented fibers density allowed MSCs and smooth muscle infiltration without disrupting the endothelial layer. Additionally, burst strength, compliance and stiffness indexes were compatible with native small diameter vessels, with the elastic modulus found to be  $323.23 \pm 99$  kPa. Nevertheless, graft thickness was only 0.15 mm instead of 1 mm of the native coronary artery, hence further optimization is needed to obtain thicker constructs. The diameter of the scaffolds manufactured were  $\approx 2$  and 4 mm, demonstrating the potential application of these constructs as coronary artery grafts in regards to this dimension.<sup>[89]</sup>

scaffold and F) a patterned electrospun scaffold with the ridge/groove width of 300/100  $\mu\text{m}$ , G) phalloidin staining of endothelial cells loaded on the random electrospun scaffold and H) smooth muscle cells on the patterned scaffold showing a preferred direction of smooth muscle cell actin fiber morphology on the patterned scaffold. Reproduced with permission.<sup>[183]</sup> Copyright 2015, Elsevier. I) SEM image of the cross section a trilayer tubular graft obtained by three-step electrospinning, J) H&E staining of cross section of transplanted constructs 2 weeks post transplantation in mice. Reproduced with permission.<sup>[185]</sup> Copyright 2018, Elsevier.

Liu et al. also reported the fabrication of a SES double layered scaffold, subsequently wrapped onto a cylinder. The outer layer was formed by SES poly(dl-lactide)–poly (ethylene glycol) (PELA) fibers which were collected on ridge-groove surfaces of 300/100 and 200/100  $\mu\text{m}$  (Figure 5F). On this layer, smooth muscle cells aligned, and actin filaments and deposited ECM increased along the circumferential direction of the grooves (Figure 5H). A second layer of random SES fibers, loaded with ECs, induced formation of a continuous endothelial layer covering the entire lumen surface (Figure 5E,G). Mechanical tests showed that the strain at failure, tensile strength and suture retention were similar to human arteries, and radial compliance and burst pressure were similar to human veins. The dimensions achieved were an inner diameter of 6 mm with an average wall thickness of  $\approx 450 \mu\text{m}$ .<sup>[183]</sup> However this is not reaching the native dimensions of  $3.54 \pm 0.51 \text{ mm}$  and  $0.89 \pm 0.21 \text{ mm}$ .<sup>[184]</sup> Wu et al. developed a trilayered semi-synthetic construct that mimic all three native layers, (Figure 5I) via a three-step SES approach. The intima-like layer was replicated by depositing axially oriented fibers (fiber diameter =  $336.90 \pm 107.27 \text{ nm}$ ) of PLCL/collagen (PLCL/COL) fibers on a 4 mm diameter mandrel. The tunica media-like layer was formed of circumferentially oriented fibers (fiber diameter =  $206.17 \pm 46.23 \text{ nm}$ ) of PLGA/silk fibroin (PLGA/SF) deposited on the PLCL/COL layer. Lastly, PLCL/COL random fibers (fiber diameter =  $361.15 \pm 136.91 \text{ nm}$ ) were deposited as adventitia. Mechanical testing revealed the trilayer tubular graft had a tensile force of  $\approx 50 \text{ N}$  with a strain of 100% in the axial direction. In vitro evaluation showed that HUVECs and smooth muscle cells aligned in the axial and circumferential fiber directions, respectively. In vivo subcutaneous implantation of the cell-free fibrous scaffold showed cell infiltration, matrix deposition and biodegradability after 10 weeks. Ten weeks after implantation the host tissue completely enclosed the scaffold, and scaffold fragments were observed (Figure 5J). Long-term mechanical stability is questionable and the degradation rate needs to be further optimized.<sup>[185]</sup>

With the combination of wet-spinning and SES, Williamson et al. created a bi-layered tubular scaffold, mimicking the different layers of the vessel. PCL was wet-spun on a 6 mm diameter rotating mandrel, and polyurethane (PU) was electrospun on top of the aligned PCL fiber cylinder and thereby achieving random, pore sizes of 10–30  $\mu\text{m}$ . HUVECs, were seeded on the PCL, secreted vascular-specific factors, and formed a cobblestone like arrangement (as described in the intima layer, Figure 1A). Human aortic smooth muscle cells were seeded on top of the porous PU layer and showed good cell attachment and proliferation. No mechanical testing was performed, so despite compatibility with two important cell types, mechanical performance remains to be investigated.<sup>[186]</sup>

Extremely important in long term in vivo (>12 months) assessment for vascular grafts is the tissue regeneration-scaffold degradation equilibrium. De Valance et al. showed promising results in vivo in a short-term follow-up of electrospun PCL-based vascular grafts whereas the long-term follow-up after implantation of the same grafts in vivo (18 months) resulted in stenotic lesions and calcification.<sup>[187]</sup> This failure was associated with the unbalanced ECM and structural support generation compared to graft degradation.<sup>[188]</sup>

To overcome these limitations, textile techniques and fast degrading polymers enable control over pore size, scaffold degradation, and tunable mechanical properties. Lui et al. braided polyglycolic acid (PGA) PGS-coated fibers into a hollow lumen, resulting in a scaffold with large enough pores for cellular integration without causing bleeding through the graft. Prior implantation the braided-scaffold showed breaking stress and radial expansion higher compared to native arteries. Six months following in vivo implantation, infiltration by host smooth muscle cells, endothelialization, deposition of ECM, and scaffold degradation was observed. Moreover, the PGS coating anti-inflammatory effect was beneficial to reduce macrophage-induced scaffold degradation. The equilibrium between tissue regeneration and graft degradation was achieved in newly formed scaffold-tissue after 3 months in vivo with ex vivo mechanical properties comparable with the native aorta.<sup>[189]</sup>

For clinically relevant applications, the use of degradable xeno-free materials has also demonstrated promising results since it ensures proper cellular adhesion and function. Kenar et al. blended xeno-free collagen types I and III, and hyaluronic acid from human umbilical cords with PCL. These semi-synthetic scaffolds resulted in a 3-fold increase in cell adhesion after 24 h, 1.6-fold longer vascular network, increased swelling and reduced elasticity (0.89 vs 1.31 MPa) compared to pure PCL scaffolds. A semi-synthetic material approach could be a promising tool for vascular graft engineering due to the significant increase in cellular response and easy manufacturing.<sup>[190]</sup>

## 5. Conclusion and Future Perspectives

We provided an overview of the recent and emerging fiber patterning technologies used for the repair of the injured myocardium, aortic valve and coronary arteries. Fiber patterning technologies have the potential to recapitulate the 3D organization of cardiac tissue on the scale of the ECM. Operating in this scale allows for a bottom-up approach in that once the original ECM structure is restored, the physical and mechanical properties can also be reestablished. Of the aforementioned techniques, SES is the technique that most closely represents the size of native ECM fibers, demonstrating the ability to guide cellular alignment and stem cell differentiation. However, due to the limited ability to create complex architectures that the ECM naturally exists in, some improvements to collecting techniques are required to facilitate the improvement of geometric design. We envision both MEW and pull spinning techniques will improve cardiac tissue repair due to their flexibility in fiber patterning geometries (box, squared, sinusoidal, hexagonal microstructures) and potential to directly create clinically relevant-sized constructs and geometries (flat/tubular/ventricle-shaped/up to 7 mm thicknesses).

It has been highlighted that for cTE of the myocardium, incorporation of natural components as supporting structures is beneficial especially in regards to degradation time matching with ECM production by the cells. This then provides the initial support until the cells have been directed into position and produce matrix. This is shown to be possible by the nanosubmicrometer sized fibers, either through SES alignment strategies or MEW microgeometries and architecture within the



construct. The next steps of this area will be to look further into composite materials that allow for both high resolution fabrication as well as some beneficial components for the tissue development, such as compounds like graphene to enhance conductivity. The biomechanics of the contraction cycle of the heart is predominately dominated by chamber pressure, while tissue stiffness dominates the relaxation cycle. This appears to be an under recognized challenge in cTE. Optimal approaches will involve constructing fiber scaffolds in which the bulk material stiffness is modulated in synchrony with the beating cycle.<sup>[191]</sup>

The development of cTE aortic valve replacement is heading in a novel direction by shifting toward porous structures on the nano- and micro-scale. This is especially important considering the high ECM fraction and specific alignment throughout the tissue layers in order to maintain its function throughout life. The aim is to make something as strong and durable as the synthetic options currently available, but with the potential to integrate with the host and function throughout development. Developing stronger materials with the ability to increase high porosity will be of importance. Additionally, manufactured fibers could have proteins immobilized to drive host cells integration.

Recent progress in mandrel collection using SES and MEW has allowed cTE for coronary arteries to advance to the stage where fiber orientation and construct morphology are showing desired functionalities. However, the key limitation with these constructs is the wall thickness which only reached half the dimensions of the native artery. These constructs in particular have addressed the design challenge of pore size allowing for cellular integration while restricting bleeding through the construct in vivo.

Up to now, long-term functionality in vivo studies of organized patterned scaffolds are still lacking and although studies conducted to date show promise for cTE, more research is required. One of the key limitations of moving toward in vivo work using these technologies is the scaling up aspect to reach physiologically and anatomically relevant constructs. The examples presented here are mostly at the stage where they could potentially be applied in a small animal model. To proceed to this next critical size level, there are a number of hurdles to overcome including the current limitations of dimensions for the micro- and nano-scale fiber production technologies, as well as the time hinderance that comes from producing such large constructs. Additionally, nutrient supply will be a consideration as these constructs become larger. Bioreactors with controllable fluid dynamics would converge very well with the field in attempts to solve this concern. Another approach is to create a prevascularized network within the constructs while in the culture phase to assist with both nutrient supply and integration with the host once in vivo. A number of groups are already moving in this direction with the main limitation of resolution as the main approach is through extrusion-based bioprinting.

Furthermore, biofabrication technologies with high resolution could be converged with the fiber fabrication technique of choice into a one-step fabrication process. For example, stereolithography technique have been utilized with photocrosslinkable hydrogels to create cell-laden structures with resolutions of 25–50  $\mu\text{m}$ .<sup>[192]</sup> SES has for instance been combined with inkjet-based 3D printing of drops of solvent ink that selectively, and with a predefined pattern, dissolves parts of the electrospun scaffold, as demonstrated by Jia et al. The desired

patterns can be based on computer-aided designs; thus, a multiphase scaffold of different patterns can be created within the nanofiber electrospun scaffolds.<sup>[193]</sup> Another example of a promising convergence of technologies is microfluidic weaving. Due to the microfluidic spinning, fibers containing cells can be generated, and when combined with weaving, these fibers can be positioned in a 3D fiber network of physiological relevant sizes.<sup>[159]</sup> Moreover, convergence of 3D (bio)printing technologies and fiber patterning can improve the manner in which cells are included within fiber constructs.

More studies need to focus on reparative integration and functional coupling to the native myocardium, valves and vessels, as well as fiber scaffold degradation and material properties modification after in vivo application. Moving close to personalized medicine, advanced imaging techniques should also be utilized in this field to progress into patient-specific tissue-engineered constructs as this would allow for the “exact” match to be calculated from patient data, creating a custom, anatomically-precise construct. To conclude, the reviewed fiber patterning techniques present great promise for cTE and their consistency, reproducibility and ECM-like resolution. The next steps of material investigation and integrative clinical solutions for these treatments is imperative and exciting for the future field of fiber formation technologies for cTE.

## Acknowledgements

M.K., M.J.A., N.C., C.F.T.v.d.V., A.v.M., and M.C. contributed equally to this work. Secondary shared authorship goes to N.C. and C.F.T.v.d.V. The authors gratefully thank the following agencies for their financial support: the strategic alliance University Medical Center Utrecht–Technical University Eindhoven, the H2020 European Research Council (ERC) (consolidator Grants 3D-JOINT, #647426 and EVICARE, #725229), the Gravitation Program “Materials Driven Regeneration” by the Netherlands Organization for Scientific Research (RegmedXB #024.003.013) and the Marie Skłodowska-Curie Actions (Grant agreement RESCUE #801540), and ReumaNederland (LLP-12). This work was also supported by the partners of Regenerative Medicine Crossing Borders (www.regmedxb.com) and powered by Health–Holland, Top Sector Life Sciences & Health.

## Conflict of Interest

The authors declare no conflict of interest.

## Keywords

cardiac regeneration, cardiac tissue engineering, extracellular matrices, fiber manufacturing technologies, fiber scaffolds, instructive biomaterials

Received: June 17, 2019  
Revised: September 14, 2019  
Published online: October 11, 2019

- [1] A. P. Ambrosy, G. C. Fonarow, J. Butler, O. Chioncel, S. J. Greene, M. Vaduganathan, S. Nodari, C. S. P. Lam, N. Sato, A. N. Shah, *J. Am. Coll. Cardiol.* **2014**, *63*, 1123.
- [2] B. Ziaieian, G. C. Fonarow, *Nat. Rev. Cardiol.* **2016**, *13*, 368.

- [3] C. E. Murry, H. Reinecke, L. M. Pabon, *J. Am. Coll. Cardiol.* **2006**, *47*, 1777.
- [4] O. Bergmann, R. D. Bhardwaj, S. Bernard, S. Zdunek, F. Barnabé-Heider, S. Walsh, J. Zupicich, K. Alkass, B. A. Buchholz, H. Druid, *Science* **2009**, *324*, 98.
- [5] A. Page, S. Messer, S. R. Large, *Ann. Cardiothorac. Surg.* **2018**, *7*, 75.
- [6] K. E. Yutzey, L. L. Demer, S. C. Body, G. S. Huggins, D. A. Towler, C. M. Giachelli, M. A. Hofmann-Bowman, D. P. Mortlock, M. B. Rogers, M. M. Sadeghi, E. Aikawa, *Arterioscler., Thromb., Vasc. Biol.* **2014**, *34*, 2387.
- [7] S. Coffey, B. Cox, M. J. A. Williams, *J. Am. Coll. Cardiol.* **2014**, *63*, 2852.
- [8] L. W. Miller, M. Guglin, J. Rogers, *Circulation* **2013**, *127*, 743.
- [9] V. Menon, J. Lincoln, *Front. Cardiovasc. Med.* **2018**, *5*, 162.
- [10] P. O. Myers, S. A. Mokashi, E. Horgan, M. Borisuk, J. E. Mayer, P. J. del Nido, C. W. Baird, *J. Thorac. Cardiovasc. Surg.* **2019**, *157*, 329.
- [11] W. Flameng, F. Rega, M. Vercalsteren, P. Herijgers, B. Meuris, *J. Thorac. Cardiovasc. Surg.* **2014**, *147*, 1219.
- [12] M. E. Soto, J. L. Salas, J. Vargas-Barron, R. Marquez, A. Rodriguez-Hernandez, R. Bojalil-Parra, I. Pérez-Torres, V. Guarner-Lans, *BMC Cardiovasc. Disord.* **2017**, *17*, 100.
- [13] E. L. Hannan, M. J. Racz, G. Walford, R. H. Jones, T. J. Ryan, E. Bennett, A. T. Culliford, O. W. Isom, J. P. Gold, E. A. Rose, *N. Engl. J. Med.* **2005**, *352*, 2174.
- [14] M. J. Byrom, M. K. Ng, P. G. Bannon, *Ann. Cardiothorac. Surg.* **2013**, *2*, 435.
- [15] Z. Niu, X. Wang, X. Meng, X. Guo, Y. Jiang, Y. Xu, Q. Li, C. Shen, *Biomed. Mater.* **2019**, *14*, 035006.
- [16] F. van den Akker, D. A. M. Feyen, P. van den Hoogen, L. W. van Laake, E. C. M. van Eeuwijk, I. Hofer, G. Pasterkamp, S. A. J. Chamuleau, P. F. Grundeman, P. A. Doevendans, *Eur. Heart J.* **2016**, *38*, 184.
- [17] P. K. Nguyen, J. W. Rhee, J. C. Wu, *JAMA Cardiol.* **2016**, *1*, 831.
- [18] J. J. H. Chong, X. Yang, C. Don, E. Minami, Y.-W. Liu, J. Weyers, W. Mahoney, B. van Biber, S. Cook, N. Palpant, J. A. Gantz, J. A. Fugate, V. Muskheli, G. M. Gough, K. W. Vogel, C. A. Astley, C. E. Hotchkiss, A. Baldessari, L. Pabon, H. Reinecke, E. A. Gill, V. Nelson, H.-P. Kiem, M. A. Laflamme, C. E. Murry, *Nature* **2014**, *510*, 273.
- [19] D. A. M. Feyen, R. Gaetani, J. Deddens, D. van Keulen, C. van Opbergen, M. Poldervaart, J. Ablas, S. Chamuleau, L. W. van Laake, P. A. Doevendans, J. P. G. Sluijter, *Adv. Healthcare Mater.* **2016**, *5*, 1071.
- [20] L. Saludas, E. Garbayo, M. Mazo, B. Pelacho, G. Abizanda, O. Iglesias Garcia, A. Raya, F. Prosper, M. J. Blanco-prieto, *J. Pharmacol. Exp. Ther.* **2019**, *370*, 761.
- [21] P. Díaz-Herráez, L. Saludas, S. Pascual-Gil, T. Simón-Yarza, G. Abizanda, F. Prósper, E. Garbayo, M. J. Blanco-Prieto, *J. Controlled Release* **2017**, *249*, 23.
- [22] W.-H. Zimmermann, I. Melnychenko, G. Wasmeier, M. Didié, H. Naito, U. Nixdorff, A. Hess, L. Budinsky, K. Brune, B. Michaelis, *Nat. Med.* **2006**, *12*, 452.
- [23] R. Madonna, L. W. Van Laake, H. E. Botker, S. M. Davidson, R. De Caterina, F. B. Engel, T. Eschenhagen, F. Fernandez-Aviles, D. J. Hausenloy, J.-S. Hulot, *Cardiovasc. Res.* **2019**, *115*, 488.
- [24] T. Shimizu, M. Yamato, Y. Isoi, T. Akutsu, T. Setomaru, K. Abe, A. Kikuchi, M. Urmez, T. Okano, *Circ. Res.* **2002**, *90*, e40.
- [25] M. Yamato, Y. Akiyama, J. Kobayashi, J. Yang, A. Kikuchi, T. Okano, *Prog. Polym. Sci.* **2007**, *32*, 1123.
- [26] D. Bejleri, B. W. Streeter, A. L. Y. Nachlas, M. E. Brown, R. Gaetani, K. L. Christman, M. E. Davis, *Adv. Healthcare Mater.* **2018**, *7*, 1800672.
- [27] M. Kitsara, O. Agbulut, D. Kontziampasis, Y. Chen, P. Menasché, *Acta Biomater.* **2017**, *48*, 20.
- [28] F. Tourlomos, C. Jia, T. Karydis, A. Mershin, H. Wang, D. M. Kalyon, R. C. Chang, *Microsyst. Nanoeng.* **2019**, *5*, 15.
- [29] T. Kuang, F. Chen, L. Chang, Y. Zhao, D. Fu, X. Gong, X. Peng, *Chem. Eng. J.* **2017**, *307*, 1017.
- [30] J. Rnjak-Kovacina, L. S. Wray, K. A. Burke, T. Torregrosa, J. M. Golinski, W. Huang, D. L. Kaplan, *ACS Biomater. Sci. Eng.* **2015**, *1*, 260.
- [31] C. H. Lee, Y. C. Lim, D. F. Farson, H. M. Powell, J. J. Lannutti, *Ann. Biomed. Eng.* **2011**, *39*, 3031.
- [32] A. Mazzoli, C. Ferretti, A. Gigante, E. Salvolini, M. Mattioli-Belmonte, *Rapid Prototyping J.* **2015**, *21*, 386.
- [33] J. Hu, D. Kai, H. Ye, L. Tian, X. Ding, S. Ramakrishna, X. J. Loh, *Mater. Sci. Eng., C* **2017**, *70*, 1089.
- [34] M. Castilho, A. van Mil, M. Maher, C. H. G. Metz, G. Hochleitner, J. Groll, P. A. Doevendans, K. Ito, J. P. G. Sluijter, J. Malda, *Adv. Funct. Mater.* **2018**, *28*, 1803151.
- [35] K. F. Eichholz, D. A. Hoey, *Acta Biomater.* **2018**, *75*, 140.
- [36] A. R. Pinto, A. Illykh, M. J. Ivey, J. T. Kuwabara, M. L. D'antoni, R. Debuque, A. Chandran, L. Wang, K. Arora, N. A. Rosenthal, M. D. Tallquist, *Circ. Res.* **2016**, *118*, 400.
- [37] X. Yang, L. Pabon, C. E. Murry, *Circ. Res.* **2014**, *114*, 511.
- [38] P. Zhou, W. T. Pu, *Circ. Res.* **2016**, *118*, 368.
- [39] S. Fleischer, T. Dvir, *Curr. Opin. Biotechnol.* **2013**, *24*, 664.
- [40] T. D. Johnson, R. C. Hill, M. Dzieciatkowska, V. Nigam, A. Behfar, K. L. Christman, K. C. Hansen, *Proteomics: Clin. Appl.* **2016**, *10*, 75.
- [41] J. P. Guyette, J. M. Charest, R. W. Mills, B. J. Jank, P. T. Moser, S. E. Gilpin, J. R. Gershlak, T. Okamoto, G. Gonzalez, D. J. Milan, G. R. Gaudette, H. C. Ott, *Circ. Res.* **2016**, *118*, 56.
- [42] T. F. Robinson, L. Cohen-Gould, S. M. Factor, M. Eghbali, O. O. Blumenfeld, *Scanning Microsc.* **1988**, *2*, 1005.
- [43] M. K. Stephenson, S. Lenihan, R. Covarrubias, R. M. Huttinger, R. J. Gumina, D. B. Sawyer, C. L. Galindo, *J. Visualized Exp.* **2016**, *112*, e54005.
- [44] G. C. Engelmayr Jr., M. Cheng, C. J. Bettinger, J. T. Borenstein, R. Langer, L. E. Freed, *Nat. Mater.* **2008**, *7*, 1003.
- [45] N. Bursac, Y. Loo, K. Leong, L. Tung, *Biochem. Biophys. Res. Commun.* **2007**, *361*, 847.
- [46] K. Dasbiswas, S. Majkut, D. E. Discher, S. A. Safran, *Nat. Commun.* **2015**, *6*, 6085.
- [47] Y. Fung, *Biomechanics: Mechanical Properties of Living Tissues*, Springer Science & Business Media, New York **1993**.
- [48] N. J. Kaiser, K. L. K. Coulombe, *Biomed. Mater.* **2015**, *10*, 034003.
- [49] P. Alter, H. Rupp, M. B. Rominger, A. Vollrath, F. Czerny, J. H. Figiel, P. Adams, F. Stoll, K. J. Klose, B. Maisch, *Mol. Cell. Biochem.* **2008**, *314*, 179.
- [50] L. Zhukov, A. H. Barr, *IEEE Visualization, 2003. VIS 2003*, IEEE, Seattle, WA **2003**, p. 597.
- [51] D. Rohmer, A. Sitek, G. T. Gullberg, *Invest. Radiol.* **2007**, *42*, 777.
- [52] A. M. S. Omar, S. Vallabhajosyula, P. P. Sengupta, *Circ.: Cardiovasc. Imaging* **2015**, *8*, 74.
- [53] D. G. León, M. López-Yunta, J. M. Alfonso-Almazán, M. Marina-Breyse, J. G. Quintanilla, J. Sánchez-González, C. Galán-Arriola, F. Castro-Núñez, J. J. González-Ferrer, B. Ibáñez, *EPP Eur.* **2019**, *21*, 822.
- [54] M. Scott, I. Vesely, *Ann. Thorac. Surg.* **1995**, *60*, S391.
- [55] M. S. Sacks, D. B. Smith, E. D. Hiester, *J. Biomed. Mater. Res.* **1998**, *41*, 131.
- [56] H. A. Eriksen, J. Satta, J. Risteli, M. Veijola, P. Väre, Y. Soini, *Atherosclerosis* **2006**, *189*, 91.
- [57] N. Latif, P. Sarathchandra, P. M. Taylor, J. Antoni, M. H. Yacoub, *J. Heart Valve Dis.* **2005**, *14*, 218.
- [58] F. J. Schoen, *J. Heart Valve Dis.* **1997**, *6*, 1.
- [59] M. S. Sacks, F. J. Schoen, J. E. Mayer, *Annu. Rev. Biomed. Eng.* **2009**, *11*, 289.

- [60] E. H. Stephens, C. K. Chu, K. J. Grande-Allen, *Acta Biomater.* **2008**, *4*, 1148.
- [61] M. Bäck, T. C. Gasser, J. B. Michel, G. Caligiuri, *Cardiovasc. Res.* **2013**, *99*, 232.
- [62] P. J. A. Oomen, S. Loerakker, D. Van Geemen, J. Neggers, M. J. T. H. Goumans, A. J. Van Den Bogaardt, A. J. J. C. Bogers, C. V. C. Bouten, F. P. T. Baaijens, *Acta Biomater.* **2016**, *29*, 161.
- [63] A. Balguid, M. P. Rubbens, A. Mol, R. A. Bank, A. J. J. C. Bogers, J. P. van Kats, B. A. J. M. de Mol, F. P. T. Baaijens, C. V. C. Bouten, *Tissue Eng.* **2007**, *13*, 1501.
- [64] I. Vesely, A. Lozon, *J. Biomech.* **1993**, *26*, 121.
- [65] D. Mavrilas, Y. Missirlis, *J. Biomech.* **1991**, *24*, 331.
- [66] D. C. Van Der Valk, C. F. T. Van Der Ven, M. C. Blaser, J. M. Grolman, P. Wu, O. S. Fenton, L. H. Lee, M. W. Tibbitt, J. L. Andresen, J. R. Wen, A. H. Ha, F. Buffolo, A. Van Mil, C. V. C. Bouten, S. C. Body, D. J. Mooney, J. P. G. Sluijter, M. Aikawa, H. Hjortnaes, R. Langer, E. Aikawa, *Nanomaterials* **2018**, *8*, 296.
- [67] J. T. Dodge Jr., B. G. Brown, E. L. Bolson, H. T. Dodge, *Circulation* **1992**, *86*, 232.
- [68] Y. Wang, S. Zeinali-Davarani, Y. Zhang, *J. Biomech.* **2016**, *49*, 2358.
- [69] J. E. Deanfield, J. P. Halcox, T. J. Rabelink, *Circulation* **2007**, *115*, 1285.
- [70] J. J. Wentzel, Y. S. Chatzizisis, F. J. H. Gijzen, G. D. Giannoglou, C. L. Feldman, P. H. Stone, *Cardiovasc. Res.* **2012**, *96*, 234.
- [71] E. W. Raines, *Int. J. Exp. Pathol.* **2000**, *81*, 173.
- [72] X. Yu, Y. Wang, Y. Zhang, *J. Mech. Behav. Biomed. Mater.* **2018**, *77*, 745.
- [73] M. K. O'Connell, S. Murthy, S. Phan, C. Xu, J. Buchanan, R. Spilker, C. A. Taylor, *Matrix Biol.* **2008**, *27*, 171.
- [74] A. L. Bauer, T. L. Jackson, Y. Jiang, *PLoS Comput. Biol.* **2009**, *5*, e1000445.
- [75] P. B. Dobrin, *Physiol. Rev.* **1978**, *58*, 397.
- [76] D. Haskett, G. Johnson, A. Zhou, U. Utzinger, J. Vande Geest, *Biomech. Model. Mechanobiol* **2010**, *9*, 725.
- [77] D. Bia, I. Aguirre, Y. Zócalo, L. Devera, E. Cabrera Fischer, R. Armentano, *Rev. Esp. Cardiol.* **2005**, *58*, 167.
- [78] C. A. Latimer, M. Nelson, C. M. Moore, K. E. Martin, *J. Surg. Res.* **2014**, *186*, 73.
- [79] G. A. Holzapfel, G. Sommer, C. T. Gasser, P. Regitnig, *Am. J. Physiol.: Heart Circ. Physiol.* **2005**, *289*, H2048.
- [80] G. C. Engelmayr Jr., M. Cheng, C. Bettinger, J. Borenstein, R. Langer, L. Freed, *Nat. Mater.* **2008**, *7*, 1003.
- [81] J. Guan, F. Wang, Z. Li, J. Chen, X. Guo, J. Liao, N. I. Moldovan, *Biomaterials* **2011**, *32*, 5568.
- [82] A. J. Engler, C. Carag-Krieger, C. P. Johnson, M. Raab, H.-Y. Tang, D. W. Speicher, J. W. Sanger, J. M. Sanger, D. E. Discher, *J. Cell Sci.* **2008**, *121*, 3794.
- [83] D. E. Discher, *Science* **2005**, *310*, 1139.
- [84] A. J. Engler, S. Sen, H. L. Sweeney, D. E. Discher, *Cell* **2006**, *126*, 677.
- [85] R. C. Lyon, F. Zanella, J. H. Omens, F. Sheikh, *Circ. Res.* **2015**, *116*, 1462.
- [86] D. E. Dostal, H. Feng, D. Nizamutdinov, H. B. Golden, S. H. Afroze, J. D. Dostal, J. C. Jacob, D. M. Foster, C. Tong, S. Glaser, F. Gerilechaogetu, *J. Clin. Exp. Cardiol.* **2014**, *5*, 314.
- [87] M. Boffito, S. Sartori, G. Ciardelli, *Polym. Int.* **2014**, *63*, 2.
- [88] G. K. Hansson, I. Kriszbacher, M. Koppán, J. Bódis, *Am. J. Pathol.* **2005**, *353*, 429.
- [89] S. Deepthi, M. Nivedhitha Sundaram, P. Vijayan, S. V. Nair, R. Jayakumar, *Int. J. Biol. Macromol.* **2018**, *109*, 85.
- [90] S. P. Hoerstrup, R. Sodian, S. Daebritz, J. Wang, E. A. Bacha, D. P. Martin, A. M. Moran, K. J. Guleserian, J. S. Sperling, S. Kaushal, J. P. Vacanti, F. J. Schoen, J. E. Mayer Jr., *Circulation* **2000**, *102*, liii-44.
- [91] B. N. Brown, S. F. Badylak, *Translating Regenerative Medicine to the Clinic, Chapter 2 - Extracellular Matrix as an Inductive Scaffold for Functional Tissue Reconstruction*, Elsevier, Amsterdam **2016**, pp. 11–29.
- [92] A. G. Guex, C. D. Spicer, A. Armgarth, A. Gelmi, E. J. Humphrey, C. M. Terracciano, S. E. Harding, M. M. Stevens, *MRS Commun.* **2017**, *7*, 375.
- [93] X. Cai, P. Zhu, X. Lu, Y. Liu, T. Lei, D. Sun, *J. Mater. Sci.* **2017**, *52*, 14004.
- [94] J. Yu, A.-R. Lee, W.-H. Lin, C.-W. Lin, Y.-K. Wu, W.-B. Tsai, *Tissue Eng., Part A* **2014**, *20*, 1896.
- [95] W. E. Teo, S. Ramakrishna, *Nanotechnology* **2005**, *16*, 1878.
- [96] X. Wang, H. Zhao, L. Turng, Q. Li, *Ind. Eng. Chem. Res.* **2013**, *52*, 4939.
- [97] F. Yang, R. Murugan, S. Wang, S. Ramakrishna, *Biomaterials* **2005**, *26*, 2603.
- [98] C. M. Rogers, G. E. Morris, T. W. A. Gould, R. Bail, S. Toumpaniari, H. Harrington, J. E. Dixon, K. M. Shakesheff, J. Segal, F. R. A. J. Rose, *Biofabrication* **2014**, *6*, 035003.
- [99] D. Zhang, J. Chang, *Nano Lett.* **2008**, *8*, 3283.
- [100] Z. Liu, F. Zhang, J. Ming, S. Bie, J. Li, B. Zuo, *J. Appl. Polym. Sci.* **2014**, *132*, 41236.
- [101] K. Jansen, M. Castilho, S. Aarts, M. M. Kaminski, S. S. Lienkamp, R. Pichler, J. Malda, T. Vermonden, J. Jansen, R. Masereeuw, *Macromol. Biosci.* **2019**, *19*, e1800412.
- [102] P. R. Sreerekha, D. Menon, S. V. Nair, K. P. Chennazhi, *Tissue Eng., Part A* **2013**, *19*, 849.
- [103] M. Asadian, S. Grande, I. Onyshchenko, R. Morent, H. Declercq, N. De Geyter, *Appl. Surf. Sci.* **2019**, *481*, 1554.
- [104] V. Moulisová, C. Gonzalez-García, M. Cantini, A. Rodrigo-Navarro, J. Weaver, M. Costell, R. Sabater I Serra, M. J. Dalby, A. J. García, M. Salmerón-Sánchez, *Biomaterials* **2017**, *126*, 61.
- [105] L. Cui, J. Li, Y. Long, M. Hu, J. Li, Z. Lei, H. Wang, R. Huang, X. Li, *RSC Adv.* **2017**, *7*, 11462.
- [106] S. Miyagawa, M. Roth, A. Saito, Y. Sawa, S. Kostin, *Ann. Thorac. Surg.* **2011**, *91*, 320.
- [107] S. H. Park, T. G. Kim, H. C. Kim, D.-Y. Yang, T. G. Park, *Acta Biomater.* **2008**, *4*, 1198.
- [108] L. Wu, H. Li, S. Li, X. Li, X. Yuan, X. Li, Y. Zhang, *J. Biomed. Mater. Res., Part A* **2010**, *92*, 563.
- [109] M. S. Islam, M. R. Karim, *Colloids Surf. A* **2010**, *366*, 135.
- [110] P. H. Chen, H. C. Liao, S. H. Hsu, R. S. Chen, M. C. Wu, Y. F. Yang, C. C. Wu, M. H. Chen, W. F. Su, *RSC Adv.* **2015**, *5*, 6932.
- [111] G. Hochleitner, A. Youssef, A. Hrynevich, J. N. Haigh, T. Jungst, J. Groll, P. D. Dalton, *BioNanoMaterials* **2016**, *17*, 159.
- [112] T. D. Brown, P. D. Dalton, D. W. Huttmacher, *Adv. Mater.* **2011**, *23*, 5651.
- [113] M. de Ruijter, A. Hrynevich, J. N. Haigh, G. Hochleitner, M. Castilho, J. Groll, J. Malda, P. D. Dalton, *Small* **2018**, *14*, 1702773.
- [114] G. Hochleitner, T. Jungst, T. D. Brown, K. Hahn, C. Moseke, F. Jakob, P. D. Dalton, J. Groll, *Biofabrication* **2015**, *7*, 035002.
- [115] F. M. Wunner, M. L. Wille, T. G. Noonan, O. Bas, P. D. Dalton, E. M. De-Juan-Pardo, D. W. Huttmacher, *Adv. Mater.* **2018**, *30*, 1706570.
- [116] N. Kawel, E. B. Turkbey, J. J. Carr, J. Eng, A. S. Gomes, W. G. Hundley, C. Johnson, C. Sofia, M. R. Prince, R. J. Van Der Geest, J. A. C. Lima, D. A. Bluemke, *Circ.: Cardiovasc. Imaging* **2012**, *5*, 500.
- [117] M. Castilho, D. Feyen, M. Flandes-Iparraguirre, G. Hochleitner, J. Groll, P. A. F. Doevendans, T. Vermonden, K. Ito, J. P. G. Sluijter, J. Malda, *Adv. Healthcare Mater.* **2017**, *6*, 1700311.
- [118] N. T. Saidy, F. Wolf, O. Bas, D. W. Huttmacher, P. Mela, E. M. De-Juan-Pardo, *Small* **2019**, *15*, 1900873.
- [119] T. D. Brown, A. Slotosch, L. Thibaudeau, A. Taubenberger, D. Loessner, C. Vaquette, P. D. Dalton, D. W. Huttmacher, *Biointerphases* **2012**, *7*, 13.
- [120] E. McColl, J. Groll, T. Jungst, P. D. Dalton, *Mater. Des.* **2018**, *155*, 46.
- [121] T. D. Brown, P. D. Dalton, D. W. Huttmacher, *Prog. Polym. Sci.* **2016**, *56*, 116.

- [122] J. N. Haigh, T. R. Dargaville, P. D. Dalton, *Mater. Sci. Eng., C* **2017**, *77*, 883.
- [123] R. Deng, Y. Liu, Y. Ding, P. Xie, L. Luo, W. Yang, *J. Appl. Polym. Sci.* **2009**, *114*, 166.
- [124] X. F. Wang, Z. M. Huang, *Chin. J. Polym. Sci.* **2010**, *28*, 45.
- [125] G. Hochleitner, J. F. Hümmer, R. Luxenhofer, J. Groll, *Polymer* **2014**, *55*, 5017.
- [126] G. Hochleitner, E. Fürsattel, R. Giesa, J. Groll, H. W. Schmidt, P. D. Dalton, *Macromol. Rapid Commun.* **2018**, *39*, 1800055.
- [127] D. Shin, J. Kim, J. Chang, *J. Manuf. Processes* **2018**, *36*, 231.
- [128] X. Li, Z. Li, L. Wang, G. Ma, F. Meng, R. H. Pritchard, E. L. Gill, Y. Liu, Y. Y. S. Huang, *ACS Appl. Mater. Interfaces* **2016**, *8*, 32120.
- [129] M. J. Madou, D. Dunn-Rankin, L. Kulinsky, A. Mirsepassi, G. S. Bisht, S. Oh, G. Canton, *Nano Lett.* **2011**, *11*, 1831.
- [130] Q. Chen, X. Mei, Z. Shen, D. Wu, Y. Zhao, L. Wang, X. Chen, G. He, Z. Yu, K. Fang, *Opt. Lett.* **2017**, *42*, 5106.
- [131] Z. Zhu, X. Chen, Z. Du, S. Huang, D. Peng, J. Zheng, H. Wang, *Mater. Manuf. Processes* **2016**, *31*, 707.
- [132] Y. K. Fuh, S. Z. Chen, Z. Y. He, *Nanoscale Res. Lett.* **2013**, *8*, 97.
- [133] X. X. He, J. Zheng, G. F. Yu, M. H. You, M. Yu, X. Ning, Y. Z. Long, *J. Phys. Chem. C* **2017**, *121*, 8663.
- [134] D. Sun, C. Chang, S. Li, L. Lin, *Nano Lett.* **2006**, *6*, 839.
- [135] G. Luo, K. S. Teh, X. Zang, D. Wu, Z. Wen, L. Lin, in *2016 IEEE 29th Int. Conf. on Micro Electro Mechanical Systems*, IEEE, Piscataway, NJ **2016**, pp. 29–32.
- [136] M. R. Badrossamay, H. A. Mcllwee, J. A. Goss, K. K. Parker, *Nano Lett.* **2010**, *10*, 2257.
- [137] M. R. Badrossamay, K. Balachandran, A. K. Capulli, H. M. Golecki, A. Agarwal, J. A. Goss, H. Kim, K. Shin, K. K. Parker, *Biomaterials* **2014**, *35*, 3188.
- [138] L. F. Deravi, H. M. Golecki, K. K. Parker, *J. Chem. Biol. Interfaces* **2013**, *1*, 25.
- [139] A. Dotivala, K. Puthuveetil, C. Tang, *Polymers* **2019**, *11*, 294.
- [140] E. S. Medeiros, G. M. Glenn, A. P. Klamczynski, W. J. Orts, L. H. C. Mattoso, *J. Appl. Polym. Sci.* **2009**, *113*, 2322.
- [141] L. F. Deravi, N. R. Sinatra, C. O. Chantre, A. P. Nesmith, H. Yuan, S. K. Deravi, J. A. Goss, L. A. MacQueen, M. R. Badrossamay, G. M. Gonzalez, M. D. Phillips, K. K. Parker, *Macromol. Mater. Eng.* **2017**, *302*, 1600404.
- [142] A. Tamayol, M. Akbari, N. Annabi, A. Paul, A. Khademhosseini, D. Juncker, *Biotechnol. Adv.* **2013**, *31*, 669.
- [143] C. Mota, D. Puppi, D. Dinucci, M. Gazzarri, F. Chiellini, *J. Bioact. Compat. Polym.* **2013**, *28*, 320.
- [144] F. Dini, G. Barsotti, D. Puppi, A. Coli, A. Briganti, E. Giannesi, V. Miragliotta, C. Mota, A. Piroso, M. R. Stornelli, P. Gabellieri, F. Carlucci, F. Chiellini, *J. Bioact. Compat. Polym.* **2016**, *31*, 15.
- [145] D. Puppi, C. Mota, M. Gazzarri, D. Dinucci, A. Gloria, M. Myrzabekova, L. Ambrosio, F. Chiellini, *Biomed. Microdevices* **2012**, *14*, 1115.
- [146] Y. Yang, J. Sun, X. Liu, Z. Guo, Y. He, D. Wei, M. Zhong, L. Guo, H. Fan, X. Zhang, *Regener. Biomater.* **2017**, *4*, 299.
- [147] Y. Yang, X. Liu, D. Wei, M. Zhong, J. Sun, L. Guo, H. Fan, X. Zhang, *Biofabrication* **2017**, *9*, 045009.
- [148] W. Qiu, W. Teng, J. Cappello, X. Wu, *Biomacromolecules* **2009**, *10*, 602.
- [149] K. Tuzlakoglu, C. M. Alves, J. F. Mano, R. L. Reis, *Macromol. Biosci.* **2004**, *4*, 811.
- [150] X. Zhang, H. Hua, X. Shen, Q. Yang, *Polymer* **2007**, *48*, 1005.
- [151] Y. Wan, X. Cao, S. Zhang, S. Wang, Q. Wu, *Acta Biomater.* **2008**, *4*, 876.
- [152] W. Jeong, J. Kim, S. Kim, S. Lee, G. Mensing, D. J. Beebe, *Lab Chip* **2004**, *4*, 576.
- [153] T. J. Kang, H. Yoon, J. H. Cheon, H. Jeong, H. Lee, Y. H. Kim, *Compos. Sci. Technol.* **2011**, *71*, 1495.
- [154] S. K. Chae, E. Kang, A. Khademhosseini, S. H. Lee, *Adv. Mater.* **2013**, *25*, 3071.
- [155] J. Oh, K. Kim, S. W. Won, C. Cha, A. K. Gaharwar, Š. Selimović, H. Bae, K. H. Lee, D. H. Lee, S.-H. Lee, *Biomed. Microdevices* **2013**, *15*, 465.
- [156] S. Cho, T. S. Shim, S. M. Yang, *Lab Chip* **2012**, *12*, 3676.
- [157] J. Cheng, Y. Jun, J. Qin, S. H. Lee, *Biomaterials* **2017**, *114*, 121.
- [158] E. Kang, G. S. Jeong, Y. Y. Choi, K. H. Lee, A. Khademhosseini, S.-H. Lee, *Nat. Mater.* **2011**, *10*, 877.
- [159] H. Onoe, T. Okitsu, A. Itou, M. Kato-Negishi, R. Gojo, D. Kiriya, K. Sato, S. Miura, S. Iwanaga, K. Kuribayashi-Shigetomi, Y. T. Matsunaga, Y. Shimoyama, S. Takeuchi, *Nat. Mater.* **2013**, *12*, 584.
- [160] S. R. Kim, H. Oh, J. Y. Baek, H. Kim, W. Kim, S. H. Lee, *Lab Chip* **2005**, *5*, 1168.
- [161] Y. Jun, E. Kang, S. Chae, S. H. Lee, *Lab Chip* **2014**, *14*, 2145.
- [162] C. M. Hwang, A. Khademhosseini, Y. Park, K. Sun, S. H. Lee, *Langmuir* **2008**, *24*, 6845.
- [163] L. Leng, A. McAllister, B. Zhang, M. Radisic, A. Günther, *Adv. Mater.* **2012**, *24*, 3650.
- [164] C. H. Yeh, P. W. Lin, Y. C. Lin, *Microfluid. Nanofluid.* **2010**, *8*, 115.
- [165] J.-H. Jung, C.-H. Choi, S. Chung, Y.-M. Chung, C.-S. Lee, *Lab Chip* **2009**, *9*, 2596.
- [166] B. R. Lee, K. H. Lee, E. Kang, D.-S. Kim, S.-H. Lee, *Biomicrofluidics* **2011**, *5*, 022208.
- [167] M. Wanjare, L. Hou, K. H. Nakayama, J. J. Kim, N. P. Mezak, O. J. Abilez, E. Tzatzalos, J. C. Wu, N. F. Huang, *Biomater. Sci.* **2017**, *5*, 1567.
- [168] D. Kai, M. P. Prabhakaran, G. Jin, S. Ramakrishna, *J. Biomed. Mater. Res., Part B* **2011**, *98B*, 379.
- [169] M. Khan, Y. Xu, S. Hua, J. Johnson, A. Belevych, P. M. L. Janssen, S. Gyorke, J. Guan, M. G. Angelos, *PLoS One* **2015**, *10*, e0126338.
- [170] C. W. Hsiao, M. Y. Bai, Y. Chang, M. F. Chung, T. Y. Lee, C. T. Wu, B. Maiti, Z. X. Liao, R. K. Li, H. W. Sung, *Biomaterials* **2013**, *34*, 1063.
- [171] S. Fleischer, A. Shapira, O. Regev, N. Nseir, E. Zussman, T. Dvir, *Biotechnol. Bioeng.* **2014**, *111*, 1246.
- [172] D. I. Zeugolis, S. T. Khew, E. S. Y. Yew, A. K. Ekaputra, Y. W. Tong, L.-Y. L. Yung, D. W. Hutmacher, C. Sheppard, M. Raghunath, *Biomaterials* **2008**, *29*, 2293.
- [173] L. A. MacQueen, S. P. Sheehy, C. O. Chantre, J. F. Zimmerman, F. S. Pasqualini, X. Liu, J. A. Goss, P. H. Campbell, G. M. Gonzalez, S.-J. Park, A. K. Capulli, J. P. Ferrier, T. F. Kosar, L. Mahadevan, W. T. Pu, K. K. Parker, *Nat. Biomed. Eng.* **2018**, *2*, 930.
- [174] O. Bas, D. D'Angella, J. G. Baldwin, N. J. Castro, F. M. Wunner, N. T. Saidy, S. Kollmannsberger, A. Reali, E. Rank, E. M. De-Juan-Pardo, D. W. Hutmacher, *ACS Appl. Mater. Interfaces* **2017**, *9*, 29430.
- [175] S. Wu, B. Duan, X. Qin, J. T. Butcher, *Acta Biomater.* **2017**, *51*, 89.
- [176] N. Masoumi, D. Copper, P. Chen, A. Cubberley, K. Guo, R. Z. Lin, B. Ahmed, D. Martin, E. Aikawa, J. Melero-Martin, J. Mayer, *Adv. Funct. Mater.* **2017**, *27*, 1606614.
- [177] R. Moreira, C. Neusser, M. Kruse, S. Mulderrig, F. Wolf, J. Spillner, T. Schmitz-Rode, S. Jockenhoevel, P. Mela, *Adv. Healthcare Mater.* **2016**, *5*, 2113.
- [178] A. Driessen-Mol, M. Y. Emmert, P. E. Dijkman, L. Frese, B. Sanders, B. Weber, N. Cesarovic, M. Sidler, J. Leenders, R. Jenni, J. Grünenfelder, V. Falk, F. P.T. Baaijens, S. P. Hoerstrup, *J. Am. Coll. Cardiol.* **2014**, *63*, 1320.
- [179] B. Weber, P. E. Dijkman, J. Scherman, B. Sanders, M. Y. Emmert, J. Grünenfelder, R. Verbeek, M. Bracher, M. Black, T. Franz, J. Kortsmid, P. Modregger, S. Peter, M. Stampanoni, J. Robert, D. Kehl, M. Doeselaar, M. Schweiger, S. P. Hoerstrup, *Biomaterials* **2013**, *34*, 7269.
- [180] O. M. J. A. Stassen, D. E. P. Muylaert, C. V. C. Bouten, J. Hjortnaes, *Curr. Treat. Options Cardiovasc. Med.* **2017**, *19*, 71.

- [181] J. Kluin, H. Talacua, A. I. P. M. Smits, M. Y. Emmert, M. C. P. Brugmans, E. S. Fioretta, P. E. Dijkman, S. H. M. Söntjens, R. Duijvelshoff, S. Dekker, M. W. J. T. Janssen-van den Broek, V. Lintas, A. Vink, S. P. Hoerstrup, H. M. Janssen, P. Y. W. Dankers, F. P. T. Baaijens, C. V. C. Bouten, *Biomaterials* **2017**, *125*, 101.
- [182] J. J. Kim, L. Hou, G. Yang, N. P. Mezak, M. Wanjare, L. M. Joubert, N. F. Huang, *Cell Mol. Bioeng.* **2017**, *10*, 417.
- [183] Y. Liu, J. Lu, H. Li, J. Wei, X. Li, *Acta Biomater.* **2015**, *11*, 114.
- [184] C. J. van Andel, P. V. Pistecky, C. Borst, *Ann. Thorac. Surg.* **2003**, *76*, 58.
- [185] T. Wu, J. Zhang, Y. Wang, D. Li, B. Sun, H. El-Hamshary, M. Yin, X. Mo, *Mater. Sci. Eng., C* **2018**, *82*, 121.
- [186] M. R. Williamson, R. Black, C. Kiely, *Biomaterials* **2006**, *27*, 1019.
- [187] E. Pektok, B. Nottelet, J. C. Tille, R. Gurny, A. Kalangos, M. Moeller, B. H. Walpoth, *Circulation* **2008**, *118*, 2563.
- [188] S. de Valence, J. C. Tille, D. Mugnai, W. Mrowczynski, R. Gurny, M. Möller, B. H. Walpoth, *Biomaterials* **2012**, *33*, 38.
- [189] T. Fukunishi, C. S. Ong, C. Lui, I. Pitaktong, C. Smoot, J. Harris, P. Gabriele, L. Vricella, L. Santhanam, S. Lu, et al., *Tissue Eng. Part A* **2019**, *25*, 632.
- [190] H. Kenar, C. Y. Ozdogan, C. Dumlu, E. Doger, G. T. Kose, V. Hasirci, *Mater. Sci. Eng., C* **2019**, *97*, 31.
- [191] I. J. Domian, H. Yu, N. Mittal, *Adv. Healthcare Mater.* **2017**, *6*, 1600768.
- [192] K. S. Lim, R. Levato, P. F. Costa, M. D. Castilho, C. R. Alcala-Orozco, K. M. A. van Dorenmalen, F. P. W. Melchels, D. Gawlitta, G. J. Hooper, J. Malda, T. B. F. Woodfield, *Biofabrication* **2018**, *10*, 034101.
- [193] C. Jia, D. Yu, M. Lamarre, P. L. Leopold, Y. D. Teng, H. Wang, *Adv. Mater.* **2014**, *26*, 8192.
- [194] D. van der Valk, C. van der Ven, M. Blaser, J. Grolman, P.-J. Wu, O. Fenton, L. Lee, M. Tibbitt, J. Andresen, J. Wen, A. H. Ha, F. Buffolo, A. Van Mil, C. V. C. Bouten, S. C. Body, D. J. Mooney, J. P. G. Sluijter, M. Aikawa, J. Hjortnaes, R. Langer, E. Aikawa, *Nanomaterials* **2018**, *8*, 296.
- [195] R. Pranjali, S. Sachin, *J. Hum. Anat.* **2018**, *2*, 000129.
- [196] F. Otsuka, A. V Finn, R. Virmani, *Atherosclerosis* **2013**, *229*, 34.
- [197] P. Gálfiová, Š. Polák, R. Mikušová, A. Gažová, D. Kosnáč, T. Barczi, J. Kyselovič, I. Varga, *Biologia* **2017**, *72*, 1521.
- [198] G. M. Gonzalez, L. A. MacQueen, J. U. Lind, S. A. Fitzgibbons, C. O. Chantre, I. Huggler, H. M. Golecki, J. A. Goss, K. K. Parker, *Macromol. Mater. Eng.* **2017**, *302*, 1600365.